

Methods to account for shallow site effects in hybrid broadband ground-motion simulations

Earthquake Spectra
I-42

© The Author(s) 2025



Article reuse guidelines:

sagepub.com/journals-permissions

DOI: 10.1177/87552930241301059

journals.sagepub.com/home/eqs



Felipe Kuncar, M.EERI¹ , Brendon A Bradley, M.EERI¹ , Christopher A de la Torre, M.EERI¹ , Adrian Rodriguez-Marek, M.EERI² , Chuanbin Zhu, M.EERI¹ , and Robin L Lee, M.EERI¹ 

Abstract

Shallow site effects are indirectly considered in conventional hybrid broadband ground-motion simulations, and their proper incorporation may be key to improving ground-motion predictions at soil sites. This article presents and examines five methods to adjust hybrid simulations to account for these effects. These methods use different approaches to modeling site response and require different amounts of site-characterization data: Methods 1 and 2 use only proxy parameters (e.g. V_{S30} , $Z_{1.0}$) to describe the site conditions, with Method 1 relying solely on proposed site response scaling factors in existing semi-empirical ground-motion models, and Method 2 incorporating a host-to-target velocity-profile adjustment; Methods 3 and 4 use a shear-wave velocity profile along with two different frequency-domain approaches to predict the linear site response, coupled with the nonlinear component of Method 1; and Method 5 uses 1D time-domain nonlinear site-response analysis and generally requires additional data to constrain nonlinear constitutive-model input parameters. The five methods are applied to four sites subjected to two levels of ground-motion intensity to illustrate the challenges involved in their implementation and to compare and contrast the resulting adjustments in terms of site amplification. The suitability and performance of each method will depend on multiple factors, including the availability of site-characterization data and complexity of the site, and hence, their relative advantages and disadvantages are discussed considering a broad range of scenarios.

¹Department of Civil and Natural Resources Engineering, University of Canterbury, Christchurch, New Zealand

²Department of Civil and Environmental Engineering, Virginia Tech, Blacksburg, VA, USA

Chuanbin Zhu is currently an Assistant Professor at the Faculty of Engineering and Environment, Northumbria University, Newcastle, UK

Corresponding author:

Felipe Kuncar, Department of Civil and Natural Resources Engineering, University of Canterbury, Private Bag 4800, Christchurch 8140, New Zealand.

Email: felipe.kuncar@pg.canterbury.ac.nz

Keywords

Site effects, hybrid broadband ground-motion simulation, ground-motion prediction, ground-motion model, square-root-impedance method, site-response analysis

Date received: 4 June 2024; accepted: 24 October 2024

Introduction

Physics-based ground-motion simulations require the modeling of source, path, and site effects. The latter refer to the influence that the local geology and geomorphology of the site have on ground shaking (Stewart et al., 2017) and include seismic wave reflection and refraction, impedance-based amplification, anelastic attenuation, and soil nonlinearity. These phenomena can significantly modify the amplitude, frequency content, and duration of the ground motion (Kramer, 1996), and hence, their proper modeling may be key to improve physics-based ground-motion predictions at soil sites, as suggested by recent validation studies (e.g. de la Torre et al., 2020; Lee et al., 2020, 2022). Whereas 3D regional-scale simulations are usually performed adopting a domain length of tens or hundreds of kilometers, which is needed to capture source and path effects, near-surface site effects occur on a scale of meters and require a finer spatial resolution in regional-scale modeling than that typically considered. Two reasons hinder the explicit incorporation of these near-surface materials in 3D regional-scale simulations: (1) the high computational cost required and (2) the lack of detailed knowledge of the near-surface material properties at the specific site of interest and in the surrounding area. These two factors are particularly important when soil nonlinearity is significant, which is typically the case for design-level ground motions.

As a result, most studies that have explicitly modeled near-surface materials in 3D regional-scale simulations, including soil nonlinearity (e.g. Dupros et al., 2010; Fu et al., 2017; Paolucci et al., 2016; Seylabi et al., 2021; Smerzini et al., 2017; Taborda et al., 2012), considered one or more simplifications: for example, (1) an idealized characterization of the sedimentary basin, represented by thick and homogeneous layers (e.g. Dupros et al., 2010; Taborda et al., 2012); or (2) a simplified modeling of soil nonlinearity, either using elastic-perfectly plastic constitutive models (e.g. Dupros et al., 2010; Fu et al., 2017; Taborda et al., 2012) or a simplified nonlinear viscoelastic approach (e.g. Paolucci et al., 2016; Smerzini et al., 2017). As an alternative, other studies have adopted an “uncoupled approach,” where the regional-scale simulation is produced without explicitly incorporating the near-surface soil materials, and the resulting ground-motion time series is adjusted to account for unmodeled local site effects. The adjustment has been performed in the frequency domain (e.g. Graves and Pitarka, 2010; Lee et al., 2022; Pilz et al., 2021; Razafindrakoto et al., 2021; Rodgers et al., 2020; Shi, 2019) and in the time domain (e.g. de la Torre et al., 2020; Evangelista et al., 2017; Hartzell, 2002; Roten et al., 2012). This modular approach does not require a significant increase in the computational effort and can make use of more localized site-characterization data. It also has all the practical benefits of making the two processes (regional-scale simulation and site effects modeling) independent, such as allowing the site-response modeling to be done at any time after the regional-scale simulation is performed (e.g. when the location-specific site-characterization data become available), or allowing different groups of professionals (i.e. engineering seismologists vs geotechnical earthquake engineers) to deal with the two parts of the problem.

However, an important limitation of this approach is that 3D site effects can be overlooked (e.g. Seylabi et al., 2021) depending on the specific implementation adopted.

Regarding the ground-motion simulation methodology, hybrid methods (e.g. Graves and Pitarka, 2010; Hartzell et al., 1999; Mai et al., 2010; Ojeda et al., 2021; Paolucci et al., 2021) are currently the most widely used in engineering applications, due to their ability to generate realistic broadband ground-motion time series in the frequency range of interest for structural and geotechnical systems (Baker et al., 2021). In this approach, the low-frequency (LF) and high-frequency (HF) components of the ground motion are simulated using different methods. The most common way in which local site effects have been considered in this methodology is through the uncoupled approach, and particularly, through a frequency-domain adjustment using site-correction factors derived from semi-empirical ground-motion models (GMMs) (e.g. Graves and Pitarka, 2010; Lee et al., 2022; Razafindrakoto et al., 2021). In this method, usually only the 30 m time-average shear-wave velocity, V_{S30} , is needed to characterize the soil conditions, which makes it particularly attractive for regional applications. However, some validation studies have shown that its use can produce systematic overestimation at long vibration periods (e.g. de la Torre et al., 2020; Lee et al., 2020, 2022). More advanced methods such as frequency-domain adjustments using 1D equivalent-linear site-response analysis (e.g. Pilz et al., 2021; Roten et al., 2012) or time-domain adjustments using 1D nonlinear site-response analysis (e.g. de la Torre et al., 2020; Roten et al., 2012; Shi, 2019) have been also explored. The latter has shown potential to improve ground-motion predictions relative to V_{S30} -based empirical site amplification, especially at complex sites (e.g. de la Torre et al., 2020), but it generally requires considerably more site-characterization data.

Although modeling of local site effects has been widely investigated in the literature as an individual component (e.g. Hallal and Cox, 2021; Kaklamanos et al., 2013), or as part of site-specific adjustments to seismic hazard analysis (e.g. NRC, 2021; Rodriguez-Marek et al., 2021; Stewart et al., 2017), relatively little attention has been given to its treatment in the context of hybrid broadband ground-motion simulations. This simulation methodology imposes specific considerations that require further examination. Specifically, questions that need to be addressed are: (1) what are the key elements for compatibility between the regional-scale simulation and subsequent site-response adjustment, and hence the theoretical attributes that the different methods to perform this adjustment should consider? (2) What are the limitations of the commonly used V_{S30} -based empirical site amplification, and what is the root cause of the overamplification at long vibration periods observed in some studies? And (3) what is the relative fidelity of different methods as a function of the amount of site-characterization data available?

This study presents a comprehensive examination of the aforementioned issues. First, the different approaches that can be used to model local site effects are examined. Second, the main aspects that must be considered to properly adjust hybrid broadband ground-motion simulations are discussed. Next, a case study is described, which is then used to discuss five methods for performing the site-response adjustment and compare the resulting site amplification factors (AFs). These methods can be applied in the presence of different levels of site-characterization data. In particular, Method 1 is the conventional V_{S30} -based approach, and Method 5 involves a time-domain adjustment based on 1D nonlinear site-response analysis; Method 2 is proposed as a modification of Method 1 to apply the site factor (SF) more consistently with ground-motion simulations; and Methods 3 and 4 are proposed as alternatives in the situation where some characterization data are available at the site, but it is still insufficient to adopt Method 5. Finally, the five methods are

compared and contrasted, and additional discussion of their utilization and limitations is provided.

Approaches for modeling local site effects

Overview

Figure 1a presents five general approaches (Approaches A–E) that can be used to model site effects in a broad range of applications (e.g. empirical or physics-based ground-motion modeling), and Figure 1b illustrates their relationship with the five methods (Methods 1–5) examined in this article, which are specifically tailored to adjusting hybrid broadband ground-motion simulations. Approaches A–E are discussed below, while the site-adjustment Methods 1–5 are described in the “Methods for performing site adjustments to hybrid broadband ground-motion simulation” section.

As illustrated in Figure 1a, going from Approach A to E implies the use of incrementally less site information and the introduction of some simplifications in the description of the site conditions and wave-propagation phenomena. Table 1 provides a comparison between these five approaches in terms of their relative advantages and disadvantages, and further discussion is provided below.

Approach A: 3D/2D time-domain site-response analysis

In this approach, the 3D or 2D wave equation is solved numerically (e.g. using finite element, finite difference, or spectral element methods) at different time steps, and soil nonlinearity is generally simulated using plasticity models (e.g. Yang et al., 2003). This method is the only one with the capability of explicitly simulating complex 3D/2D wave-propagation features such as basin effects (e.g. Ayoubi et al., 2021) or wave scattering due to soil heterogeneities (e.g. de la Torre et al., 2022a; Thompson et al., 2009), offering the highest potential to realistically simulate site effects among the approaches presented in Figure 1a. However, this would involve significant challenges in the model characterization, such as data collection within a great lateral extension (e.g. Hallal and Cox, 2023) or the definition of random-field (e.g. de la Torre et al., 2022b) and spatially distributed nonlinear parameters. Furthermore, defining an input motion on the model boundaries that adequately reflects the spatial variability of the incident wavefield can be challenging. This approach is not considered in the methods examined in this study to adjust ground-motion simulations.

Approach B: 1D time-domain site-response analysis

The numerical simulation in this approach relies on the 1D wave-propagation assumptions: the medium is represented by laterally continuous and homogeneous layers overlying a half-space; wavefronts are considered to be planar; and only horizontally polarized shear waves propagating in the vertical direction are modeled (the so-called SH1D assumptions). In addition to plasticity models, simpler cyclic stress-strain relationships (e.g. Groholski et al., 2016; Shi and Asimaki, 2017) can be used to capture soil nonlinearity. Adopting the SH1D assumptions has two implications: (1) it allows the problem to be represented with a relatively simple site-response model, and using site-characterization data (e.g. geophysical and cone penetration tests [CPTs]) that are typically collected within a relatively small area, corresponding to the site of interest, and (2) sites with conditions that violate these

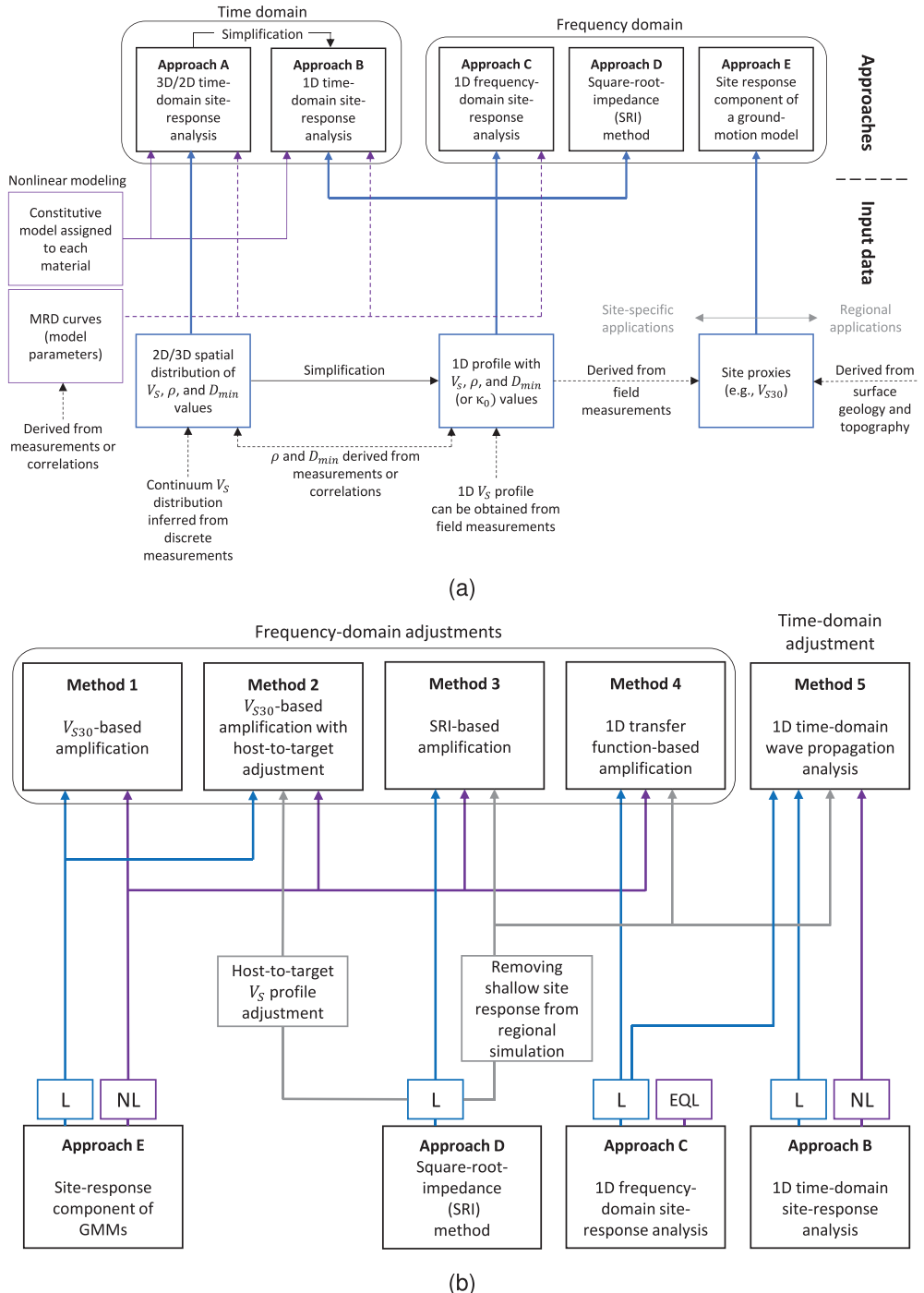


Figure 1. (a) Time-domain and frequency-domain approaches to model site effects, and their respective input data. (b) The relationship between these approaches and the investigated methods to perform site adjustments to hybrid broadband ground-motion simulations. L: linear; NL: nonlinear; EQL: equivalent-linear.

Table 1. Comparison of different approaches to model site effects

Approach	Pros	Cons
A. 3D/2D time-domain site-response analysis	3D/2D wave-propagation effects and soil nonlinearity can be explicitly modeled	Requires more site-characterization data than is usually available Significant computational cost and analyst competency Performance diminishes when the 1D SH-wave propagation (SHID) assumptions do not hold
B. 1D time-domain site-response analysis	1D wave-propagation effects and soil nonlinearity can be explicitly modeled Required site-characterization data can be collected at a reasonable cost compared to Approach A	Advanced constitutive models require the calibration of multiple parameters Performance diminishes when the SHID assumptions do not hold Limitations to model soil nonlinearity It can underpredict site response when resonance effects are relevant It is not able to model soil nonlinearity
C. 1D frequency-domain site-response analysis	Linear 1D wave-propagation effects are explicitly modeled Required site-characterization data can be collected at a reasonable cost compared to Approach A	
D. Square-root-impedance method	Site-specific impedance and attenuation effects are modeled Required site-characterization data can be collected at a reasonable cost compared to Approach A Computed site	
E. Site response component of ground-motion models	amplification is not sensitive to the details in the shear-wave velocity (V_s) profile (which is generally characterized by considerable levels of uncertainty) 3D wave-propagation effects (consistent with the sites considered in the GMM development) are implicitly captured Requires considerably less site-characterization data and analyst competency than Approaches A–D	Characterization via proxy parameters (e.g., V_{s30}) may ignore site-specific features Biased predictions if appropriate host-to-target adjustment is not considered

assumptions can result in inaccurate ground-motion predictions, as shown by several validation studies (e.g. Afshari and Stewart, 2019; Kaklamanos et al., 2013; Pilz and Cotton, 2019; Thompson et al., 2009, 2012; Zhu et al., 2022). As illustrated in Figure 1b, this approach is used in Method 5.

Approach C: 1D frequency-domain site-response analysis

This approach also relies on the SH1D assumptions. However, in this case, the problem is solved in the frequency domain through the direct application of a complex-valued transfer function, TF_{SH1D} , to the Fourier transform of the input motion (ground motion at a reference condition, that needs to be propagated through the soil column). Alternative methods are available to compute TF_{SH1D} for a given configuration of horizontal soil layers over an elastic half-space (e.g. Haskell, 1953; Kramer, 1996; Thomson, 1950). This complex transfer function (TF) accounts for both the modification of the amplitude and the phase of the input motion. The equivalent-linear (EQL) method (Seed and Idriss, 1969) is typically used to consider soil nonlinearity if necessary. This method has been widely adopted in engineering practice due to its simplicity but presents some limitations such as the overdamping (i.e. underprediction) of ground motion at high frequencies when the soil experiences relatively large shear strains (e.g. Kaklamanos et al., 2013; Kim et al., 2016). As shown in Figure 1b, this approach is used in Methods 4 and 5.

Approach D: square-root-impedance method

This seismological approach combines the square-root-impedance (SRI) method (Boore, 2003, 2013; Joyner et al., 1981) to model site amplification, $I(f)$, with a diminution operator, $D(f)$, to capture site attenuation (Anderson and Hough, 1984). The resulting “outcrop” TF, $TF_{SRI}(f)$, can be applied in the same way as in Approach C:

$$TF_{SRI}(f) = I(f)D(f) = \sqrt{\frac{\rho_R V_{S,R}}{\bar{\rho} \bar{V}_S}} \exp(-\pi f \kappa_0) \quad (1)$$

where ρ_R and $V_{S,R}$ are the density (ρ) and shear-wave velocity (V_S), respectively, at the reference condition; $\bar{\rho}$ and \bar{V}_S are the corresponding average ρ and travel-time weighted average V_S , respectively, computed at each frequency, f , considering a depth equivalent to the quarter-wavelength; and κ_0 is the site attenuation parameter (Anderson and Hough, 1984; Ktenidou et al., 2014) estimated at the surface. The diminution operator can also account for a portion of κ_0 , corresponding to the contribution of the near-surface materials down to a reference horizon (e.g. Cabas and Rodriguez-Marek, 2017), in which case, κ_0 is replaced by $\Delta\kappa_0$ in Equation 1, where $\Delta\kappa_0 = \kappa_0 - \kappa_{0,R}$ (being $\kappa_{0,R}$ the value estimated at the reference horizon). Approach D does not account for soil nonlinearity.

Several differences exist between TF_{SRI} (Approach D) and TF_{SH1D} (Approach C): (1) TF_{SRI} does not consider any phase adjustment, which is accounted for in TF_{SH1D} ; (2) the amplification term in TF_{SRI} represents only impedance effects and does not account for resonance effects (Thompson et al., 2011; Zhu et al., 2022), which are explicitly modeled in TF_{SH1D} ; (3) the attenuation model is conceptually different, resulting in lower levels of damping for TF_{SRI} in the case of a one-layer system when equivalent attenuation parameters are used for TF_{SH1D} and TF_{SRI} (Boore, 2013); and (4) TF_{SRI} is significantly less sensitive to details in the V_S profile than TF_{SH1D} (Boore, 2013). Due to aspect (2), TF_{SH1D}

produces peaks and troughs in the TF, with significant amplification over narrow frequency bands, which are absent in TF_{SRI} . The existence of these resonant features strongly depends on the suitability of the SH1D assumptions and the considered horizontal stratigraphy, as well as stiffness and damping properties. Soil heterogeneity and other non-1D wave phenomena can prevent, or significantly reduce, their development (e.g. de la Torre et al., 2022a; Thompson et al., 2011). Due to several sources of uncertainty that exist in the estimation of the V_S profile (Rodriguez-Marek et al., 2021), aspect (4) means that important levels of uncertainty can be also expected in the computation of TF_{SH1D} (Thompson et al., 2011). Boore and Abrahamson (2023) proposed a modification to the SRI approach that gives results closer to TF_{SH1D} for gradient profiles, but it is not explored in this article. As illustrated in Figure 1b, this Approach D is used in Methods 2, 3, 4, and 5.

Approach E: site response component of a GMM

Semi-empirical GMMs (Baker et al., 2021, Ch. 4) provide a prediction of the mean value of a given intensity measure (IM) in natural log scale, for an earthquake rupture, rup , and the site considered, *site*, with the general form,

$$\mu_{\ln IM}(rup, site) = f_E + f_P + f_S \quad (2)$$

where f_E , f_P , and f_S are source, path, and site response scaling factors, respectively. In the context of this article, two IMs will be primarily considered: pseudo-spectral acceleration (SA) and Fourier amplitude spectra (FAS). The site response scaling factor (f_S) can be generally expressed as the sum of three terms (e.g. Bayless and Abrahamson, 2019; Campbell and Bozorgnia, 2014):

$$f_S = f_L + f_{NL} + f_{sed} \quad (3)$$

where f_L and f_{NL} represent the scaling of the linear and nonlinear site response, respectively, with one or more site parameters (e.g. V_{S30}). In addition, the term f_{NL} is a function of some IM at a reference condition (IM_{rock}). For example, the CB14 model (Campbell and Bozorgnia, 2014) uses the estimated median value of peak ground acceleration (PGA) on rock with $V_{S30} = 1100$ m/s. The term f_{sed} represents the scaling with the thickness of the site column, with V_S lower than a certain threshold value. This is typically characterized by the parameter $Z_{1.0}$, corresponding to the depth to a Vs of 1.0 km/s (e.g. Bayless and Abrahamson, 2019; Boore et al., 2014), although some GMMs (e.g. Campbell and Bozorgnia, 2014) use $Z_{2.5}$ (depth to 2.5 km/s) instead. The f_{sed} term can also depend on V_{S30} when the scaling factor is based on the relationship between $Z_{1.0}$ and the average $Z_{1.0}$ expected for a given region computed using a V_{S30} -based correlation (e.g. Bayless and Abrahamson, 2019; Boore et al., 2014).

The terms f_L , f_{NL} , and f_{sed} are based on observational ground-motion data, theoretical models, and numerical simulations. In particular, due to the lack of recordings with strong soil nonlinearity, several models have been developed for f_{NL} using a large number of 1D site-response analyses (e.g. Hashash et al., 2018; Kamai et al., 2014; Shi, 2019; Walling et al., 2008) or combining these analyses with observations (e.g. Seyhan and Stewart, 2014), and they are implemented in different GMMs. Most of these models represent only an adjustment to the amplitude of the ground motion in the Fourier or response spectral domain, but a phase adjustment can also be included (e.g. Shi, 2019: Ch.4). As shown in Figure 1b, this approach is used in Methods 1, 2, 3, and 4.

Hybrid broadband ground-motion simulation methodology

Overview

Currently, 3D numerical ground-motion simulations of the earthquake source and (3D) wave propagation are utilized in engineering applications only up to a limited maximum frequency of $f = 1\text{--}3$ Hz (Graves and Pitarka, 2016; Paolucci et al., 2021). This is primarily due to knowledge limitations regarding small-scale features of the fault rupture and the Earth's crust (Graves and Pitarka, 2016; Mai et al., 2010) and is compounded by the large computational demands of simulating small length scales. As a result, hybrid simulation methods have been applied (e.g. Graves and Pitarka, 2010; Mai et al., 2010), which utilize this comprehensive 3D physics-based approach for the LF simulation and a simplified physics-based approach for the HF simulation. The resulting LF and HF waveforms are then combined using a matched filter around a transition frequency, f_t . The transition frequency f_t often corresponds to 1 Hz but generally is increasing over time as computation, theory, and velocity models improve.

The method developed by Graves and Pitarka (2010, 2015, 2016) (herein referred to as the GP method for brevity) has been applied and validated in different regions, including California, Europe, and New Zealand (e.g. Dreger et al., 2015; Lee et al., 2022; Razafindrakoto et al., 2021) and is considered in this article to illustrate the challenges in the modeling of shallow site effects in hybrid broadband simulations. In this method, the LF component is simulated using a kinematic description of the earthquake fault rupture and a visco-elastic finite-difference algorithm to solve the 3D wave propagation equation. The HF component is simulated using a stochastic representation of source radiation and a simplified Green's function determined for a given 1D velocity structure. In particular, a frequency-dependent quality factor (Q) is used to incorporate path anelastic attenuation, and the SRI method along with the multiplicative operator $P(f) = \exp(-\pi f \kappa_{0,\text{sim}})$ (Approach D) is used to represent impedance effects and capture HF spectral decay, where $\kappa_{0,\text{sim}}$ is the site attenuation parameter considered in the simulation. Further details on the implementation of this method in this study are provided in Razafindrakoto et al. (2018) and Lee et al. (2022).

Considerations for the modeling of shallow site effects

The modeling of shallow site effects in hybrid broadband ground-motion simulations is usually performed using the “uncoupled approach” (e.g. de la Torre et al., 2020; Graves and Pitarka, 2010; Pilz et al., 2021; Razafindrakoto et al., 2021), and therefore, it takes the form of a posterior adjustment to the ground-motion time series produced by the regional-scale simulation. The four main aspects that need to be considered when performing this adjustment are discussed below.

First, the hybrid nature of the simulation method requires different considerations for the adjustment of the LF and HF components. For example, in the case of the GP method, the 3D velocity structure considered in the LF approach allows for the incorporation of any level of spatial variability within the simulation domain, whereas the HF approach is usually performed using a unique 1D velocity profile representative of the whole region of interest (e.g. Graves and Pitarka, 2010; Lee et al., 2022). Consequently, the 1D velocity profile implicit in the LF and HF components of the simulated ground motions at a given site can be significantly different, including the minimum V_S ($V_{S,\text{min}}$).

Second, due to knowledge and computational limitations, the minimum V_S considered in the regional-scale simulation typically corresponds to a stiff soil or rock condition (e.g. $V_{S,min} = 500$ m/s in Lee et al., 2022), and the spatial variations of V_S are represented with a relatively coarse resolution (e.g. a constant grid spacing of 100 m was considered for the LF simulation in Lee et al., 2022). In reality, near-surface materials typically reach lower values and exhibit significant spatial variation in V_S within the top 100 m. Thus, site effects adjustments should be able to capture these features not modeled in the regional simulation.

Third, although near-surface sediments are generally not properly modeled in the regional-scale simulation (e.g. due to the high $V_{S,min}$ value and coarse grid spacing in Lee et al., 2022), local site effects may be captured to some extent. For instance, “basin effects” (Ayoubi et al., 2021) may be dominated by the deep velocity structure of the site, which can be relatively well represented in the LF component of the simulation (e.g. a relatively well-constrained 3D crustal velocity model of the Canterbury Region is considered in the LF simulation conducted by Lee et al., 2022), even if the shallower sedimentary layers are coarsely represented. Another example is related to the HF site attenuation, which is modeled in the HF component of the simulation through the parameter κ_0 (e.g. $\kappa_{0,sim} = 0.045$ s was used in Lee et al., 2022). Both “basin effects” and HF attenuation are already incorporated in the regional simulation to some degree, which must be taken into account when applying the site response adjustment, to avoid double-counting them.

Finally, regional-scale simulations are usually performed considering linear viscoelastic materials (e.g. Graves and Pitarka, 2010; Lee et al., 2022). Hence, the adjustment has to model soil nonlinearity, which is particularly relevant for maximum shear strains $\gamma_{max} > 0.01\%–0.1\%$ (e.g. Kaklamanos et al., 2013). While several 3D ground-motion simulations have explicitly included non-linear near-surface response (e.g. Fu et al., 2017; Taborda et al., 2012), such simulation results are still limited by the minimum spatial scale challenges alluded to above, as well as the ability to represent site-specific near-surface stratigraphy *a priori* in the regional simulation (as opposed to a posterior adjustment via an uncoupled approach which allows for site-specific data collection and site-response analysis for regional simulations that already have been performed).

Case study

General description

A case study is considered to examine the different methods to adjust ground-motion simulations and compare and contrast their features. It includes four strong motion station (SMS) sites in Christchurch, New Zealand, for which site characterization data (e.g. Teague et al., 2018; Wotherspoon et al., 2015) and simulation results of historical events (Lee et al., 2022; Razafindrakoto et al., 2018) are available. Table 2 shows that the four sites represent a wide range of site conditions. $V_{S30,actual}$ and $Z_{1.0,actual}$ are the measured or inferred values from the preferred V_S profile available at each location. In the case of PRPC and CACS, the measured V_S profile was relatively shallow, and it did not reach 1000 m/s, so the New Zealand Velocity Model (NZVM) (Thomson et al., 2020), version 2.07, was used to estimate $Z_{1.0,actual}$. Z_G is the depth to the first gravel formation, which in the central and eastern part of Christchurch corresponds to the Riccarton Gravel Formation and represents a significant velocity contrast relative to the softer sediments above (Teague et al., 2018; Wotherspoon et al., 2015). Based on these parameters, PRPC and CMHS represent relatively soft sites; with CMHS a shallower soil deposit (i.e. smaller

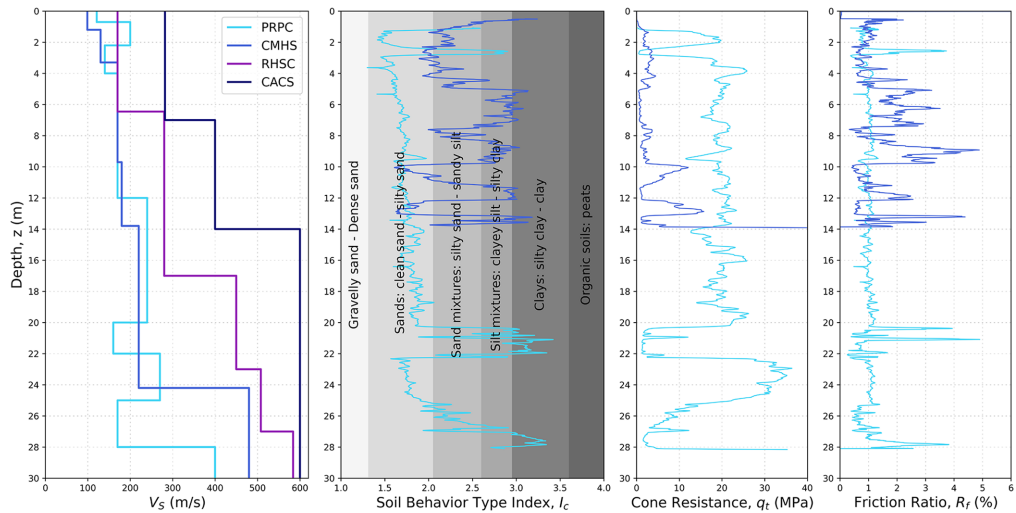


Figure 2. V_s profiles and CPT data used for the four sites considered.

Z_G and $Z_{1.0,actual}$ values), consistent with its location near the basin edge (see Supplemental Figure A.1 in Electronic Supplement A). RHSC and CACS are stiffer sites, with CACS an example where the gravel formation starts at the surface.

A low- and a high-intensity ground motion are considered for each site in order to examine the different methods in the near-linear and nonlinear response regimes. The associated events are described in Electronic Supplement A. Only one horizontal component of these ground motions is used.

Site-characterization data

Figure 2 presents the V_s profile (via surface-wave testing) and CPT data used to characterize the four sites considered, down to 30 m. As observed in the soil behavior type index (I_c) plot, in the top 28 m, the site PRPC is mainly characterized by clean and silty sands, with some localized layers of more cohesive materials; whereas in the top 13.8 m, the site CMHS has a more variable stratigraphy, with a greater presence of cohesive soils. For RHSC and CACS, CPT data were not available, but boreholes and standard penetration test (SPT) data were considered. Further details and site data available at these four locations are provided in Wotherspoon et al. (2015), Teague et al. (2018), and Electronic Supplement A.

Ground-motion simulations considered

The events considered in this case study were simulated using the GP method. The simulations of the low-intensity events were performed by Lee et al. (2022), and those of the high-intensity event by Razafindrakoto et al. (2018). For the LF component, the NZVM (Thomson et al., 2020) v2.02 with a grid spacing of 100 m and a minimum $V_s = 500$ m/s was utilized. For the HF component, the nationwide 1D velocity model described in Lee

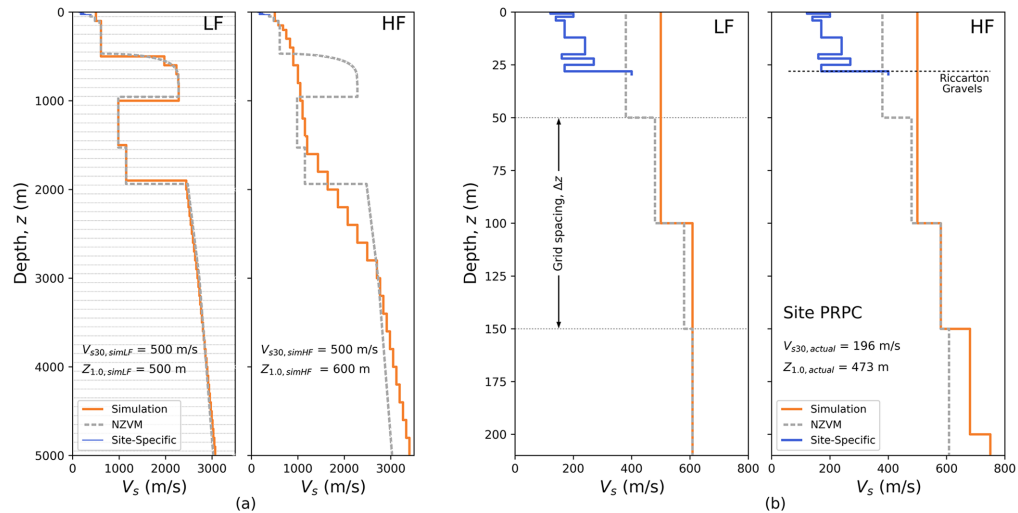


Figure 3. Site-specific, LF simulation, HF simulation, and NZVM (v2.07) V_s profiles at PRPC. The horizontal dashed lines represent the grid spacing considered in the LF simulation: (a) 0–5000 m deep. (b) 0–220 m deep.

Table 2. Parameters representative of the actual and simulation site conditions for the four sites considered

Site	Actual site conditions			Simulation site conditions		
	$V_{s30,actual}$ (m/s)	Z_G (m)	$Z_{1,0,actual}$ (m)	$V_{s30,sim}$ (LF and HF) (m/s)	$Z_{1,0,simLF}$ (m)	$Z_{1,0,simHF}$ (m)
PRPC	196	28	473	500	500	600
CMHS	203	14	57	500	100	600
RHSC	294	6.5	555	500	400	600
CACS	435	0.0	557	500	600 (*)	600

Z_G is the depth to the first gravel formation. The $Z_{1,0}$ values of the LF and HF simulations differ due to the differences in the 3D and 1D velocity structures used.

(*) The V_s value actually reached at the 600-m depth is 0.98 km/s, which remains constant down to 1200-m depth, where V_s increases to 1.15 km/s. Because of this particular stratigraphy, 600 m was chosen as a more meaningful value for $Z_{1,0,simLF}$.

et al. (2022) was used, which also considers a minimum $V_s = 500$ m/s. The transition frequency between LF and HF components was set to $f_t = 1$ Hz.

Figure 3a shows the 1D V_s profile extracted at the site PRPC from the 3D velocity model used in the LF simulation, and the corresponding HF V_s profile (herein, the LF and HF simulation profiles), illustrating that the two profiles have different deep velocity structures. The LF profile captures a localized volcanic formation that produces strong V_s contrasts at depths of 500 m and 1000 m. These velocity contrasts do not appear in the HF profile, which is a regional average representation. Figure 3b illustrates the common case where the regional-scale LF and HF simulations are not able to accurately capture the V_s of the surficial soil, which is typically characterized by $V_s < 500$ m/s with significant variation at a scale of meters. Table 2 provides the site parameters V_{s30} and $Z_{1,0}$.

associated with the simulation conditions for the LF and HF components. Similar figures for all the sites are provided in Electronic Supplement A.

Methods for performing site adjustments to hybrid broadband ground-motion simulations

Overview

In this section, five methods to perform the site adjustment are presented, and the case study sites are used to illustrate their application and compare the methods under different soil conditions. As shown in Figure 1b, these methods are based on a range of different approaches discussed in the “Approaches for modeling local site effects” section; in particular, Approaches B–E. Approach A was not considered in this study because its use in engineering applications is limited. For example, even though the sites considered in the case study are well-characterized near the SMS, proper implementation of Approach A would require spatially distributed data over a considerably larger area (Hallal and Cox, 2023), and these data are significantly sparser. Also, defining an input motion that is compatible with the regional-scale ground-motion simulation is challenging. While methods exist that allow determining the equivalent input forces derived from 3D ground-motion simulations (e.g. Bielak, 2003), their implementation requires significant analyst competency and dealing with the hybrid nature of the simulation method.

The site adjustment can be performed in the frequency domain (Methods 1–4) or in the time domain (Method 5). The “frequency-domain adjustment” involves five steps:

1. Obtaining the simulated acceleration time series at the surface of the site of interest, $a_{sim}(t)$. This corresponds to the regional ground-motion simulation without any adjustment for shallow site effects.
2. Computing the discrete Fourier transform (DFT) of $a_{sim}(t)$ via the fast Fourier transform (FFT) algorithm.
3. Determining the SF to be applied to account for shallow site effects. SF is defined as a function of frequency, and Methods 1–4 represent different formulations to obtain it. In these methods, only an amplitude adjustment is considered (i.e. the phase of the simulated ground motion is not modified), but a phase adjustment can also be included (e.g. Pilz et al., 2021; Shi, 2019), which would account for the time delay of the seismic waves when propagating through the soil deposit. This phase adjustment could be relevant in the analysis of spatially distributed infrastructure (Shi, 2019: Ch.4).
4. Applying the SF to the DFT of $a_{sim}(t)$.
5. Obtaining the adjusted acceleration time series (which accounts for shallow site effects), $a_{adj}(t)$, via the inverse fast Fourier transform (IFFT) algorithm.

Since the simulated acceleration time series are different for the LF and HF components, the adjustment is performed separately for each component, and then the adjusted LF and HF time series are combined in the time domain. This procedure is described in the “Application of the site factor” section of Electronic Supplement B. Given that the simulation profiles are also different for each component, this may result in different LF and HF SFs. In the following sections describing Methods 1–4, the LF and HF SFs are only plotted in their associated frequency ranges ($f < 1$ Hz and $f > 1$ Hz, respectively), but it

should be noted that when they are applied to the simulated ground motions, their influence slightly exceed these frequency ranges in the vicinity of $f = 1$ Hz, due to the low- and high-pass filters applied before merging, which ensure a smooth transition. Also, due to the differences alluded to earlier, the LF and HF SFs may not perfectly match at $f = 1$ Hz, which manifests as a discontinuity in some of the figures presenting the SFs.

The “time-domain adjustment” involves the use of time-domain site response analysis. Method 5 corresponds to a specific implementation of this approach, based on 1D non-linear inelastic site-response analysis, and it is further explained in the “Method 5 - 1D time-domain wave propagation analysis” section.

The site PRPC is first used to explain the methods, but results for all four case study sites are provided in Electronic Supplement C and in the “Comparison of the site amplification obtained with the five methods” section.

Method 1— V_{S30} -based amplification

This method uses the site response scaling factor (f_S) from existing semi-empirical GMMs (Approach E) and corresponds to the method used in Graves and Pitarka (2010) to capture shallow site effects. In principle, the computation of the SF (SF_1) is based on the ratio between the median prediction of the FAS for the actual site conditions (FAS_{actual} , and the corresponding prediction for the simulation site conditions (FAS_{sim}):

$$SF_1(f) = \frac{\exp[\mu_{\ln FAS_{actual}(f)}]}{\exp[\mu_{\ln FAS_{sim}(f)}]} \quad (4)$$

Since semi-empirical models for FAS have only recently been developed (e.g. Bayless and Abrahamson, 2019; Bora et al., 2019), several previous studies have used GMMs for SA to approximately compute SF_1 instead (e.g. Graves and Pitarka, 2010; Lee et al., 2022). Due to the differences between SA and FAS (Bora et al., 2016), SF_1 estimates based on SA models have been truncated to a value of 1 at high frequencies to mitigate the inconsistencies between the two IMs (e.g. as discussed in de la Torre et al., 2020).

Since source and path effects are common to the numerator and denominator in Equation 4, it reduces to the ratio of site terms. Specifically:

$$SF_1(f) = \frac{\exp[f_{S, actual}(f)]}{\exp[f_{S, sim}(f)]} = \frac{\exp(f_{L, actual} + f_{NL, actual} + f_{sed, actual})}{\exp(f_{L, sim} + f_{NL, sim} + f_{sed, sim})} \quad (5)$$

where all terms have been previously defined in the “Approach E: Site response component of a ground-motion model” section. The terms $f_{sed, actual}$ and $f_{sed, sim}$ may or may not be included in Equation 5. For example, Graves and Pitarka (2010), who used the CB08 model (Campbell and Bozorgnia, 2008), did not include them, arguing that the effect of deep-basin amplification was already included in their LF simulation. If the regional ground-motion simulation is performed adopting a linear viscoelastic constitutive model, which is usually the case, the term $f_{NL, sim}$ should in principle be removed from Equation 5. This has been considered in some studies (e.g. Rodgers et al., 2020), but others (e.g. Lee et al., 2022) have not removed this term. Considering that usually $f_L \sim f(V_{S30})$, $f_{NL} \sim f(V_{S30}, IM_{rock})$, and $f_{sea} \sim f(V_{S30}, Z_{1.0})$, Equation 5 can be rewritten as,

Table 3. Recent ground-motion simulation studies that have used Method I

Study	Simulation method	GMM used for computing SF(f)	Implementation
Shi (2019), Ch.4 Southern California, US	Hybrid (Graves and Pitarka, 2010) $f_t = 1 \text{ Hz}$, $V_{s,min}$ as implemented in the SCEC Broadband Platform (BBP) v17.3.0	Combination of BSSA14 (Boore et al., 2014) and CB14 (Campbell and Bozorgnia, 2014) IM: SA SAG19 (Shi, 2019: Ch.4) IM: FAS	As implemented in the SCEC BBP v17.3.0 Different from Equation 5
Lee et al. (2020) Canterbury, New Zealand	Hybrid (Graves and Pitarka, 2010) $f_t = 1 \text{ Hz}$, $V_{s,min} = 500 \text{ m/s}$	CB14 (Campbell and Bozorgnia, 2014) IM: SA	Not including f_{sed} Truncation at LF and HF
Rodgers et al. (2020) Northern California, US	3D numerical simulation $f_{max} = 10 \text{ Hz}$, $V_{s,min} = 500 \text{ m/s}$	BA18 (Bayless and Abrahamson, 2019) IM: FAS	Including f_{sed} Without truncations
Razafindrakoto et al. (2021) Upper Rhine Graben, Europe	Hybrid (Graves and Pitarka, 2010) $f_t = 1 \text{ Hz}$, $V_{s,min} = 800 \text{ m/s}$	CB14 (Campbell and Bozorgnia, 2014) IM: SA BCS19 (Bora et al., 2019) IM: FAS	Not including f_{sed} Truncation at LF and HF Without truncations
Lee et al. (2022) New Zealand	Hybrid (Graves and Pitarka, 2010) $f_t = 1 \text{ Hz}$, $V_{s,min} = 500 \text{ m/s}$	CB14 (Campbell and Bozorgnia, 2014) IM: SA	Not including f_{sed} Only applied to the HF component, with HF truncation

$$SF_1(f) = \frac{\exp[f_L(f, V_{S30,actual}) + f_{NL}(f, V_{S30,actual}, IM_{rock}) + f_{sed}(f, V_{S30,actual}, Z_{1.0,actual})]}{\exp[f_L(f, V_{S30,sim}) + f_{sed}(f, V_{S30,sim}, Z_{1.0,sim})]} \quad (6)$$

This results in a SF that can be expressed as,

$$SF_1(f) = SF_{1,L}(f) \cdot SF_{1,NL}(f) \quad (7)$$

where $SF_{1,L} = \exp(f_{L,actual} + f_{sed,actual} - f_{L,sim} - f_{sed,sim}) \sim f(V_{S30,actual}, Z_{1.0,actual}, V_{S30,sim}, Z_{1.0,sim})$ is the linear component of SF_1 , and $SF_{1,NL} = \exp(f_{NL,actual}) \sim f(V_{S30,actual}, IM_{rock})$ is the non-linear component. Several studies have truncated this SF to a value of $SF_1 = 1$ at low frequencies to avoid double-counting LF amplification already captured in the LF simulation component, based on a 3D velocity model (e.g. Graves and Pitarka, 2010; Lee et al., 2020, 2022). The IM_{rock} parameter generally corresponds to the PGA at a certain reference V_{S30} that varies between GMMs. Here, the PGA obtained from the HF simulation (HF PGA) at $V_{S30,sim}$ is used and scaled to the model-dependent reference V_{S30} , applying a linear SF based on the corresponding GMM. This procedure is explained in more detail in Electronic Supplement B.

Table 3 summarizes some of the most recent studies on ground-motion simulations where Method 1 has been used to capture site effects. The table illustrates that there is no consistent approach to date to implement Method 1, and subjective decisions are involved in the selection of the GMM, the application of LF and HF truncations, and the inclusion of the f_{sed} terms.

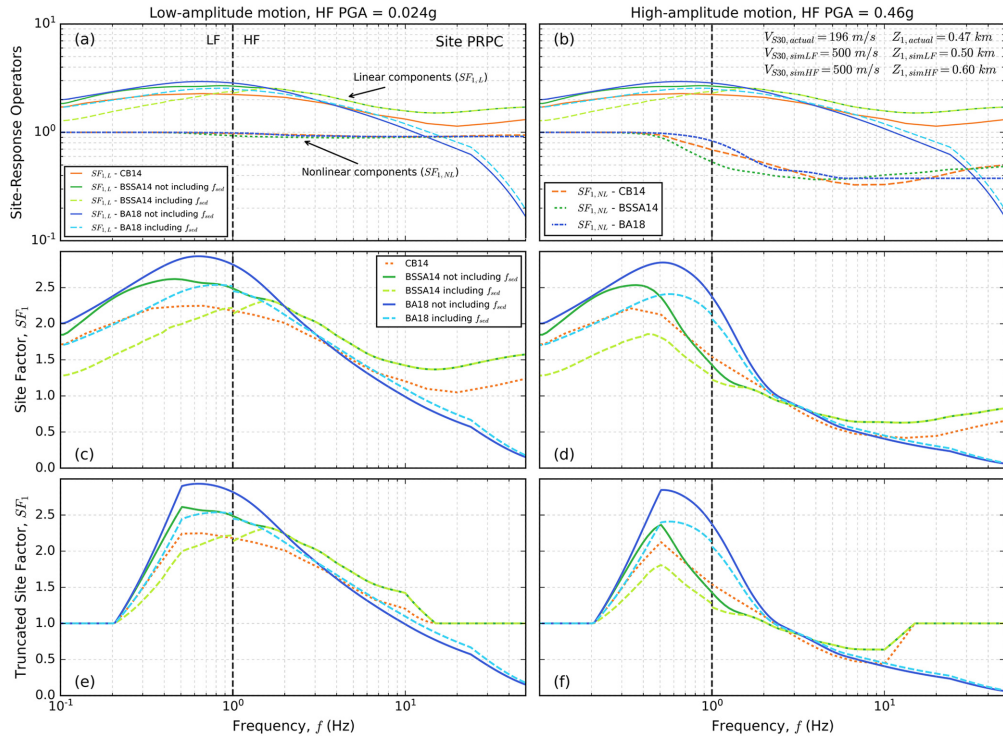


Figure 4. Site factors obtained for the site PRPC using Method I and different models: (a) and (b) Show the linear and nonlinear components for the low-amplitude and high-amplitude motion, respectively. (c) and (d) Present the resulting site factors without any truncations. (e) and (f) Show the site factors with LF and HF truncations.

In order to illustrate the implications of alternative combinations of models, Figure 4 presents the resulting SFs (SF_1) for the site PRPC. This comparison comprises two models developed in the response spectral domain (CB14, BSSA14) and one model developed in the Fourier spectral domain (BA18), which have been used in previous studies (Table 3). In the case of the BSSA14 and BA18 models, the results are presented with and without the $f_{sed}(f, V_{S30}, Z_{1.0})$ terms ($f_{sed, actual}$ and $f_{sed, sim}$), to illustrate the effect that this model component has on the SF. Further details of the models considered and additional results including the BCS19 and SAG19 models are provided in Electronic Supplements B and C, respectively.

Figures 4a and b display the linear ($SF_{1,L}$) and nonlinear ($SF_{1,NL}$) components of the SFs for the two events considered; Figures 4c and d present the resulting SFs (SF_1) without any truncations; and Figures 4e and f show the SFs with two truncations applied: (1) for all the models, the LF SF is truncated to a value of $SF_1 = 1$ for $f < 0.2$ Hz with a taper from $f = 0.5$ – 0.2 Hz, as considered in some previous studies (e.g. de la Torre et al., 2020; Lee et al., 2020; Razafindrakoto et al., 2021); and (2) in the case of the SA-based models (CB14, BSSA14), the HF SF is truncated to a value of $SF_1 = 1$ for $f > 15$ Hz, with a taper from $f = 10$ – 15 Hz, as also considered in some previous studies (e.g. de la Torre et al., 2020; Lee et al., 2020, 2022; Razafindrakoto et al., 2021).

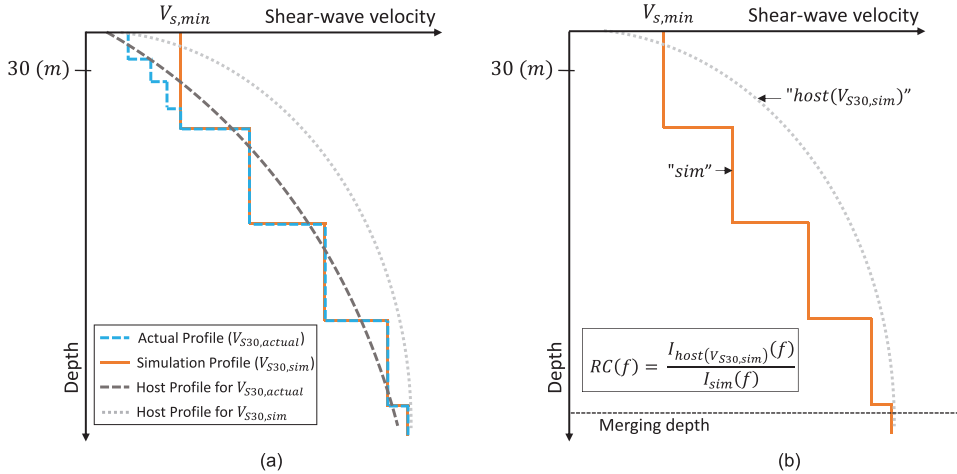


Figure 5. (a) Illustration of the host-to-target conversion issue present in Method 1. (b) Computation of the reference correction (RC) factor introduced in Method 2.

Significant model-to-model variability is observed in the linear and nonlinear components of the SF in Figures 4a and b, but in the latter case, this variability only manifests under the high-amplitude ground motion (Figure 4b). For the low-amplitude motion, the nonlinear component of the three GMMs is close to unity over the entire frequency range, whereas for the high-amplitude motion, this component substantially departs from 1 at frequencies greater than 0.5 Hz, resulting in de-amplification. These figures also show that the BA18 model accounts for the HF decay in the site response, a feature that cannot be properly captured in the response spectral domain (Bora et al., 2016; Cabas and Rodriguez-Marek, 2017).

A common feature observed in all the SFs, clearly illustrated in Figures 4c and d, is the relatively high amplification at low frequencies, particularly around $f = 0.3\text{--}1.0$ Hz. This amplification is reduced when the f_{sed} terms are included in the BSSA14 and BA18 models. This is mainly driven by an increase in the $\exp(f_{sed,sim})$ term at low frequencies, as explained in the “Effect of f_{sed} on $SF_{1,L}$ ” section of Electronic Supplement C. Several validation studies conducted in New Zealand (de la Torre et al., 2020; Lee et al., 2020, 2022), for example, have shown that this high amplification may lead to significant overprediction in the LF range, even when an LF truncation is applied. Considering this, Lee et al. (2022) showed that the application of the SF to the HF component only (i.e. $f > 1$ Hz) can significantly reduce the model bias at long vibration periods. One of the downsides of this approach is that the proper truncation may be site- and region-dependent.

Host-to-target adjustment issue

To investigate the root cause of the apparent overamplification at relatively low frequencies, Figure 5a illustrates a V_S profile representing the actual site conditions (actual profile) at a hypothetical soil site, with an associated $V_{S30,actual}$ value. It also shows the corresponding simulation profile, which is assumed to be equivalent to the actual profile in the deeper portion (i.e. the deep velocity structure is well represented by the regional-scale simulation) but differs in the shallow portion because the regional-scale simulation is conducted

truncating the V_S profile to a $V_{S,min}$ value, due to computational and knowledge constraints (e.g. $V_{S,min} = 500$ m/s in the case study considered in this article). This results in $V_{S30,sim} = V_{S,min}$. Under these conditions, the purpose of the SF should be to capture the site response generated by the actual profile relative to the simulation profile (due to the near-surface soil layers characterized by lower velocities in the actual profile) and accounting for soil nonlinearity. As discussed before, the determination of the site response in Method 1 is based on a GMM and one or more proxy parameters, such as V_{S30} . For a given GMM and V_{S30} value, there is a corresponding theoretical V_S profile which reflects the implicit site conditions considered in the development of the GMM, which is referred to as the “host” V_S profile (Al Atik and Abrahamson, 2021; Baker et al., 2021: Ch. 8). Figure 5a includes the host profiles associated with $V_{S30,actual}$ and $V_{S30,sim}$ for a hypothetical GMM.

Figure 5a illustrates that a significant inconsistency may exist between the “target” condition to be modeled (i.e. relative site response between the actual and simulation profile) and the “host” condition implicit in the SF SF_1 (i.e. relative site response between the two host profiles). In the context of empirical ground-motion modeling and site-specific seismic hazard analysis, this problem is known as the host-to-target adjustment issue (e.g. Bard et al., 2020; Campbell, 2003; NRC, 2021; Williams and Abrahamson, 2021). In the specific case of Method 1, there are three main related issues:

1. Inconsistency between the simulation profile and the host profile for $V_{S30,sim}$: As outlined in Figure 5a, the host profiles for $V_{S30,actual}$ and $V_{S30,sim}$ will generally display significant differences at depth (especially if $V_{S30,actual}$ departs considerably from $V_{S30,sim}$), due to the positive correlation that usually exists between V_{S30} and V_S at depth in a typical geological environment (Boore et al., 2011; Kamai et al., 2016). The same correlation will not exist in the case of the simulation profile because its V_{S30} value results from an artificial truncation to $V_{S30,sim} = V_{S,min}$, rather than being an inherent profile property (e.g. $V_{S30,actual}$ better correlates with the simulation profile at depth than $V_{S30,sim}$). If $V_{S30,actual} < V_{S30,sim}$, as in Figure 5a, the host profile for $V_{S30,sim}$ will tend to be significantly stiffer at depth than the simulation profile, which will generate overamplification at relatively low frequencies when SF_1 is computed. This aligns with previous observations in some validation studies.
2. Inconsistency between the actual profile and the host profile for $V_{S30,actual}$: As illustrated in Figure 5a, the actual profile may also differ from the host profile for $V_{S30,actual}$, although these differences may be less significant than for the simulation ($V_{S30,sim}$) condition. Using a region-specific model (e.g. Nweke et al., 2022) calibrated for the region where the simulation is performed should help to mitigate this issue.
3. Double-counting deep 3D velocity structure effects: If the ground-motion simulation is conducted using a high-quality 3D velocity model for the LF component, it will be possible to capture 3D amplification phenomena, including basin effects, which means that the SF does not have to account for them. However, since the host profile for $V_{S30,sim}$ generally represents a stiff (near-rock) condition at depth, where basin effects are limited or absent, and the host profile for $V_{S30,actual}$ represents a site condition where these effects are present, the net effect will be the inclusion of them in SF_1 . This will potentially result in double-counting 3D effects already captured by the LF simulation, increasing the LF overamplification in

Method 1, which is the reason given in some previous studies for truncating SF_1 at low frequencies (e.g. Graves and Pitarka, 2010; Lee et al., 2022).

Method 2— V_{S30} -based amplification with host-to-target adjustment

In Method 2, a host-to-target adjustment is proposed to partially overcome the inconsistency involved in Method 1. Particularly, this adjustment addresses the first issue explained in the previous section (“Host-to-target adjustment issue”), related to the difference between the simulation profile and the host profile for $V_{S30, sim}$. This method is inspired by previous studies that have suggested similar adjustments but in different contexts (e.g. Cabas and Rodriguez-Marek, 2017; NRC, 2021; Williams and Abrahamson, 2021). Method 2 is a V_S correction approach based on the SRI method (Approach D), which allows for adjusting the Method 1 SF (SF_1) to minimize the incompatibility between the simulation profile and site condition implicit in the GMM for $V_{S30, sim}$. More specifically, the Method 2 SF (SF_2) can be expressed as,

$$SF_2(f) = \frac{\exp[f_{S, actual}(f)]}{\exp[f_{S, sim}(f)]} \cdot \frac{I_{host(V_{S30, sim})}(f)}{I_{sim}(f)} = SF_1(f) \cdot RC(f) \quad (8)$$

where $I_{host(V_{S30, sim})}$ and I_{sim} are the SRI-based site amplifications for the host V_S profile associated with $V_{S30, sim}$ and for the simulation profile, respectively; RC is the reference correction factor. The computation of this factor is illustrated in Figure 5b and is conducted using the following equation:

$$RC(f) = \frac{I_{host(V_{S30, sim})}(f)}{I_{sim}(f)} = \frac{\sqrt{\frac{\rho_R V_{S,R}}{\bar{\rho}_{host(V_{S30, sim})} V_{S, host(V_{S30, sim})}}}}{\sqrt{\frac{\rho_R V_{S,R}}{\bar{\rho}_{sim} V_{S, sim}}}} \quad (9)$$

where the subscripts $host(V_{S30, sim})$ and sim indicate properties of the host profile for $V_{S30, sim}$ and of the simulation profile, respectively; and ρ_R and $V_{S,R}$ are the density and V_S , respectively, at a reference depth common to the two profiles, considered as the elastic half-space. Figure 5b indicates the depth at which the two profiles merge. The half-space can be located at this location or deeper. This reference correction factor intends to ensure consistency with the host profile for $V_{S30, sim}$, but it does not address the potential inconsistency with the host profile for $V_{S30, actual}$, which is a common limitation of any ergodic method based on V_{S30} (for Methods 1 and 2, it is assumed that the only site information available is $V_{S30, actual}$).

The main challenge for the application of Method 2 is deriving the host profile implicit in the GMM(s) considered for $V_{S30, sim}$. As discussed by Williams and Abrahamson (2021), there are two approaches to estimate this profile if the GMM developers do not provide it: (1) assuming that available measurements of V_S within the region for which the GMM was developed are representative of the host profile (e.g. Kamai et al., 2016), and (2) deriving the profile from the GMM by solving the inverse problem (e.g. Al Atik and Abrahamson, 2021). In this study, the host profiles derived by the Al Atik and Abrahamson (2021) method for the CB14 and BSSA14 models are considered. Al Atik and Abrahamson (2021) showed that the profiles derived with their method (for four NGA-West2 GMMs) provide a better match with the site response implicit in the GMMs for very stiff site conditions (e.g. $V_{S30} = 620$ m/s or greater), which are less influenced by 2D/3D effects. They

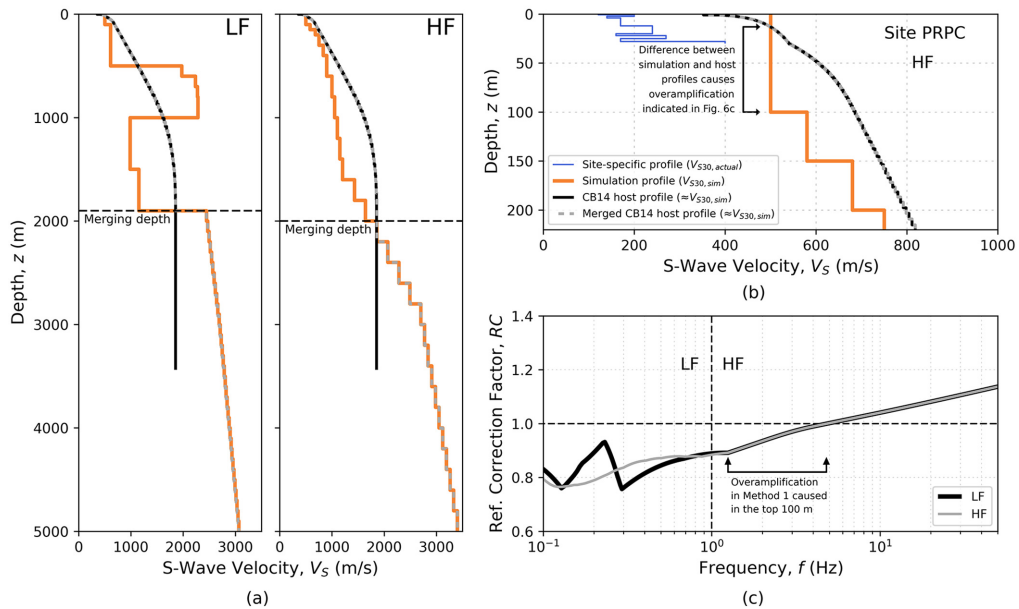


Figure 6. Reference adjustment in Method 2 for the site PRPC: (a) LF and HF profiles, from 0 to 5000 m; (b) HF profiles from 0 to 220 m; and (c) resulting reference correction factors.

showed that for lower V_{S30} values, the method was less effective. The inversion was originally based on the SRI method, but the use of a modified version of the SRI method proposed by Boore and Abrahamson (2023) improves the results for $V_{S30} = 490$ m/s in the shallow portion of the host profiles (L. Al Atik, personal communication, April 6, 2023). The updated profiles for $V_{S30} = 490$ m/s (which represent a condition very close to $V_{S30,sim} = 500$ m/s) were provided by L. Al Atik and are used here to illustrate the application of Method 2.

Figure 6 presents the computation of the reference correction factor for the site PRPC, considering the CB14 model (results for the BSSA14 model are provided in Electronic Supplement C). As shown in Figure 6a, the different LF and HF simulation profiles result in slightly different merging depths at each frequency range. Given that the accuracy of the host profile estimation reduces with depth, this profile was modified to be equivalent to the simulation profile below the selected merging depth. The reference depth for the calculating RC was defined at 5000 m.

Figure 6c shows that the resulting reference correction factor is less than 1 for $f < 5$ Hz, reducing the amplification (i.e. mitigating the overprediction issue) at relatively low frequencies in Method 1. Interestingly, Figure 6c reveals that the overamplification issue in Method 1 is not restricted to the LF component but also affects part of the HF range. As illustrated in Figures 6b and c, this is due to the difference between the HF simulation profile and the host profile for $V_{S30,sim}$ in the top ≈ 100 m. Although both profiles are characterized by $V_{S30,sim}$, the HF simulation profile displays a constant value of $V_S = 500$ m/s down to a depth of 100 m, whereas the host V_S increases with depth to a value close to 700 m/s, generating increasing levels of overamplification in Method 1 from $f \approx 5$ Hz to $f \approx 1.2$ Hz, as can be seen in Figure 6c. This overamplification is removed

by Method 2, through the application of RC . For $f > 5$ Hz, RC is positive, which is due to the host V_S values < 500 m/s at the very shallow depths. However, this has limited effect on SF_2 because a HF truncation is considered for the CB14 and BSSA14 models (developed in the response spectral domain) in the same fashion as in Method 1. The resulting SF_2 and its comparison with SF_1 are investigated in the “Comparison of the site amplification obtained with the five methods” section and in Electronic Supplement C.

Method 3—SRI-based amplification

Methods 1 and 2 only require proxy parameters (e.g. V_{S30} , $Z_{1.0}$) to characterize the site conditions, which on many occasions is the only information available (e.g. in regional applications). If more site-specific site-characterization data exist, alternative approaches can be used. Method 3 uses a V_S profile and the SRI method (Approach D) to represent the linear component of the SF, as follows:

$$SF_{3,L}(f) = \frac{TF_{SRI,actual}}{TF_{SRI,sim}} = \frac{\sqrt{\frac{\rho_R V_{S,R}}{\bar{\rho}_{actual} V_{S,actual}}}}{\sqrt{\frac{\rho_R V_{S,R}}{\bar{\rho}_{sim} V_{S,sim}}}} \cdot \frac{\exp[-\pi f \kappa_{0,actual}]}{\exp[-\pi f \kappa_{0,sim}]} \quad (10)$$

where the subscripts *actual*, *sim*, and *R* indicate properties of the actual profile, simulation profile, and reference condition (i.e. elastic half-space considered for the amplification computation), respectively; and in particular, $\kappa_{0,actual}$ and $\kappa_{0,sim}$ are the HF site attenuation parameters estimated at the top of the actual and simulation profiles, respectively.

The objective of the denominator in Equation 10 is to remove the impedance- and attenuation-based site response introduced by the regional ground-motion simulation within the depth over which the site adjustment is considered. The use of the SRI method in this equation is fully consistent with the treatment of the linear amplification and HF attenuation adopted in the HF ground-motion simulation method (as described in the “Hybrid broadband ground-motion simulation methodology” section). Although the LF simulation is based on a different approach (3D time-domain wave propagation), the frequencies affected by $TF_{SRI,sim}$ are mainly in the HF range (i.e. $f > 1$ Hz) for shallow site adjustments of concern here. Nonetheless, as the transition frequency of hybrid ground motion simulations increases over time (e.g. $f_t \gg 1$ Hz), a more consistent approach for the LF range could be adopted.

Equation 10 can be rewritten as

$$SF_{3,L}(f) = \sqrt{\frac{\bar{\rho}_{sim} \bar{V}_{S,sim}}{\bar{\rho}_{actual} \bar{V}_{S,actual}}} \cdot \exp[-\pi f (\kappa_{0,actual} - \kappa_{0,sim})] = SF_{3,L,I}(f) \cdot SF_{3,L,D}(f) \quad (11)$$

where $SF_{3,L,I}$ and $SF_{3,L,D}$ are the amplification and attenuation operators for the $SF_{3,L}$ factor. $SF_{3,L,I}$ represents the relative linear (impedance-based) site amplification between the actual and simulation profiles with respect to a common elastic half-space, and $SF_{3,L,D}$ represents the relative site attenuation between the actual and simulation site conditions. Since κ_0 reflects the cumulative effect of damping through the full site profile (Afshari and Stewart, 2019; Campbell, 2009), the term $(\kappa_{0,actual} - \kappa_{0,sim})$ in Equation 11 accommodates any difference in the amount of damping represented by $\kappa_{0,actual}$ and $\kappa_{0,sim}$, for a theoretical material column that can extend to a depth significantly greater than the near-surface

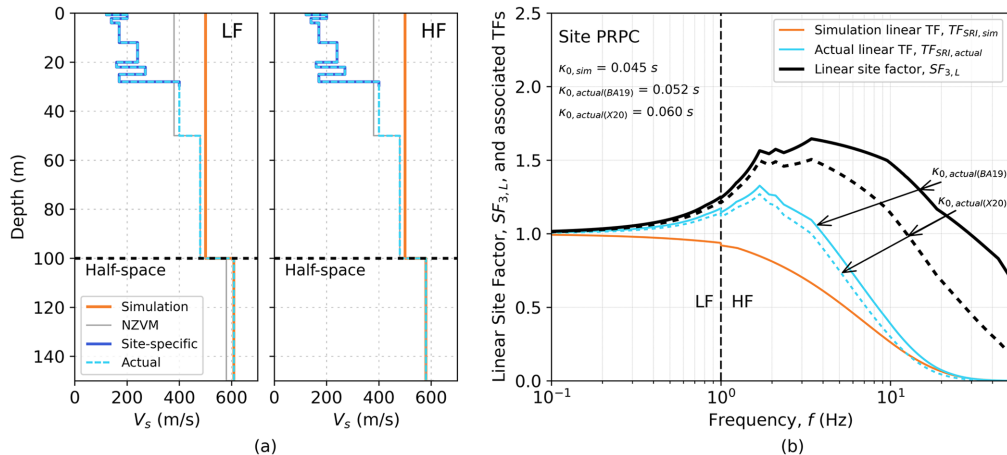


Figure 7. (a) V_S profiles used in Methods 3 (and subsequently, in Method 4), for the site PRPC. (b) Resulting linear site factor.

(e.g. deeper than 100 m). In contrast, the amplification operator, $SF_{3,L,I}$, is generally limited to capturing impedance effects in the near-surface (e.g. within the top 100 m), where site-specific V_S data are most likely to be available.

Since Equation 11 (i.e. Approach D) is limited to the estimation of the linear site response, the nonlinear operator derived in Method 1 is proposed for capturing soil nonlinearity in Method 3. In this way, the total SF in Method 3 (SF_3) is computed as

$$SF_3(f) = SF_{3,L}(f) \cdot SF_{1,NL}(f) \quad (12)$$

Figure 7 illustrates the computation of the linear component of Method 3 for the site PRPC. Figure 7a shows the derivation of the actual V_S profile and the selection of the elastic half-space. The definition of the half-space in this method requires that the actual and simulation profiles merge at a certain depth; however, the available site-specific V_S profile for PRPC has a depth of 30 m and does not reach the simulation profile. To achieve this, alternative sources of information can be utilized to extend the site-specific profile to a proper depth. The V_S profile extracted from the NZVM (without imposing a minimum V_S) is used, and the half-space is selected at a depth of 100 m. Given that for Method 3, it is assumed that the only site information available is the $V_{S,actual}$ profile, the actual soil density, ρ_{actual} , is estimated using the V_S -based correlation for unit weight provided in Rix et al. (2019).

Since the HF ground-motion simulation methodology uses the SRI method in the same fashion as Method 3, $\kappa_{0,sim}$ is a known input parameter. In particular, $\kappa_{0,sim} = 0.045$ s was used in all the regional simulations considered in this article. When this value is used in Equation 10, the generic HF spectral decay considered in the regional HF simulation is fully removed and replaced by a site-specific estimate based on $\kappa_{0,actual}$. $\kappa_{0,actual}$ can be estimated using a number of different methods (e.g. Ktenidou et al., 2014), including its direct derivation from recordings and the use of correlations with V_{S30} and other site parameters. In this study, $\kappa_{0,actual}$ is estimated using two different V_{S30} -based correlations, proposed by Bayless and Abrahamson (2019) and Xu et al. (2020), which give values of

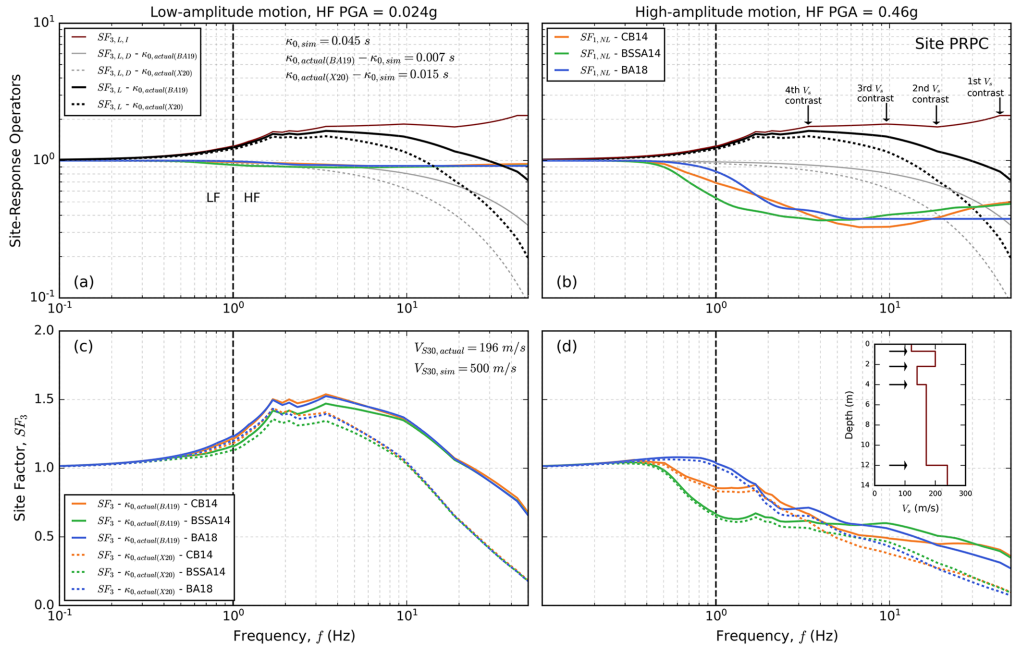


Figure 8. (a) Site-response operators of Method 3 for the site PRPC considering the low-amplitude motion, (b) the high-amplitude motion, (c) resulting site factors for the low-amplitude motion, and (d) high-amplitude motion.

$\kappa_{0,actual}(BA19) = 0.052$ s and $\kappa_{0,actual}(X20) = 0.060$ s, respectively, for PRPC. It must be acknowledged that κ_0 - V_{S30} correlations generally present significant scatter (e.g. Ktenidou et al., 2014), with a standard deviation in natural log units in the order of 0.30 (e.g. Xu et al., 2020). Figure 7b presents the linear SFs from Method 3 (Equation 11) for the two estimates of $\kappa_{0,actual}$, along with the linear site response associated with the actual ($TF_{SRI,actual}$) and simulation ($TF_{SRI,sim}$) profiles. The figure shows that the selection of $\kappa_{0,actual}$ has a greater impact at higher frequencies, especially for $f > 4$ Hz. In particular, the frequency at which $SF_{3,L}$ starts displaying deamplification vary significantly, with $f \sim 13$ Hz for $\kappa_{0,actual}(X20)$ and $f \sim 30$ Hz for $\kappa_{0,actual}(BA19)$.

Figure 8 presents the SFs (SF_3), along with the underlying operators, $SF_{3,L,I}$, $SF_{3,L,D}$, and $SF_{1,NL}$, for the low-amplitude and high-amplitude motions, considering three alternative GMMs for the computation of $SF_{1,NL}$. Figure 8b shows that changes in the slope of the linear amplification operator ($SF_{3,L,I}$) are associated with the presence of additional velocity contrasts (shown in the inset within Figure 8d) in its computation, illustrating the direct relationship between depth and frequency in the SRI method. Particularly, the linear amplification at frequencies greater than 3 Hz is controlled by the top 12 m of the soil profile. Figures 8a and c show that in the case of the low-amplitude motion, the selection of the κ_0 model generally has a greater impact than the choice of the nonlinear model ($SF_{1,NL}$). However, Figures 10b and d indicate that for the high-amplitude motion, the selection of the nonlinear model has a greater influence in the frequency range $0.5 < f < 2.5$ Hz, and the sensitivity to the estimation of $\kappa_{0,actual}$ starts to dominate at $f > 10$ Hz.

Method 4—1D TF-based amplification

Method 4 is similar to Method 3 but uses the theoretical 1D TF (Approach C) to account for linear site effects. The linear component of the SF can be expressed as follows:

$$SF_{4,L}(f) = \frac{|TF_{SH1D,actual}(V_{S,actual}, \rho_{actual}, D_{min,actual})|}{\sqrt{\frac{\rho_R V_{S,R}}{\rho_{sim} V_{S,sim}}} \cdot \exp[-\pi f \Delta \kappa_{0,sim}]} \quad (13)$$

where the numerator represents the linear site response for the actual profile, computed through the modulus of the outcrop 1D TF ($TF_{SH1D,actual}$), and the denominator represents the linear site response for the simulation profile ($TF_{SRI,sim}$), with respect to a common elastic half-space (more details regarding this are provided in the “Definition of the reference condition in Method 4” section of Electronic Supplement B). Since the objective of the denominator is to remove the site response introduced by the regional ground-motion simulation, the SRI method is used in the denominator of Equation 13 for consistency with the HF ground-motion simulation (similar to Method 3). In Method 4, this is implemented in the same fashion as the $V_S - \kappa_0$ deconvolution approach proposed by Cabas and Rodriguez-Marek (2017). $\Delta \kappa_{0,sim}$ is defined as $\Delta \kappa_{0,sim} = \kappa_{0,sim} - \kappa_{0,R}$, where $\kappa_{0,sim}$ and $\kappa_{0,R}$ are the HF site attenuation parameters estimated at the top of the simulation profile and at the top of the elastic half-space, respectively. The elastic half-space, and the actual and simulation V_S profiles, are established in the same way as in Method 3 (see Figure 7a).

In the same manner as in Method 3, nonlinearity is modeled in Method 4 using the nonlinear operator from Method 1. Hence, the total SF in Method 4 (SF_4) is computed as

$$SF_4(f) = SF_{4,L}(f) \cdot SF_{1,NL}(f) \quad (14)$$

Other studies have also utilized theoretical 1D TFs to adjust hybrid broadband ground-motion simulations (e.g. Ojeda et al., 2021; Pilz et al., 2021), but either they have not accounted for soil nonlinearity (e.g. Ojeda et al., 2021) or have used a different approach to model it, such as the equivalent linear method (e.g. Pilz et al., 2021). The method proposed here to treat nonlinearity along with the linear amplification from the 1D TF is simpler and only requires V_{S30} for the nonlinear component.

Several approaches have been proposed to estimate the small-strain damping D_{min} (e.g. Afshari and Stewart, 2019; Cabas et al., 2017; Darendeli, 2001; Pretell et al., 2023; Xu et al., 2020), which can be used in Method 4 to compute $D_{min,actual}$. Here, three formulations are investigated: (1) a laboratory-based damping, $D_{min,actual}^{lab}$, computed using Darendeli (2001); (2) $D_{min,actual}^{lab}$ with a multiplicative factor of 3 (Pretell et al., 2023); and (3) a V_S -based damping, $D_{min,actual}^S$, computed via $D_{min} = 1/(2Q)$ (Kramer, 1996), where the quality factor, Q , is estimated using $Q = 7.17 + 0.0276V_S$ (Campbell, 2009, Model 1), with V_S in m/s. The multiplicative factor considered in (2) is based on the recognition that the intrinsic material damping measured in the laboratory (D_{min}^{lab}) does not fully capture the actual damping observed in the field due to additional mechanisms such as wave scattering (Afshari and Stewart, 2019; Cabas et al., 2017; de la Torre et al., 2022a), which results in the overprediction of the theoretical fundamental mode when D_{min}^{lab} is used (Pretell et al., 2023). The multiplicative factor should be ideally determined on a site-specific basis, which is possible, for example, in the case of borehole array sites (e.g. Afshari and Stewart, 2019; Xu et al., 2020). A generic value of 3 is used in this study based on Pretell et al. (2023), who found that this factor improves the overall site response prediction at multiple

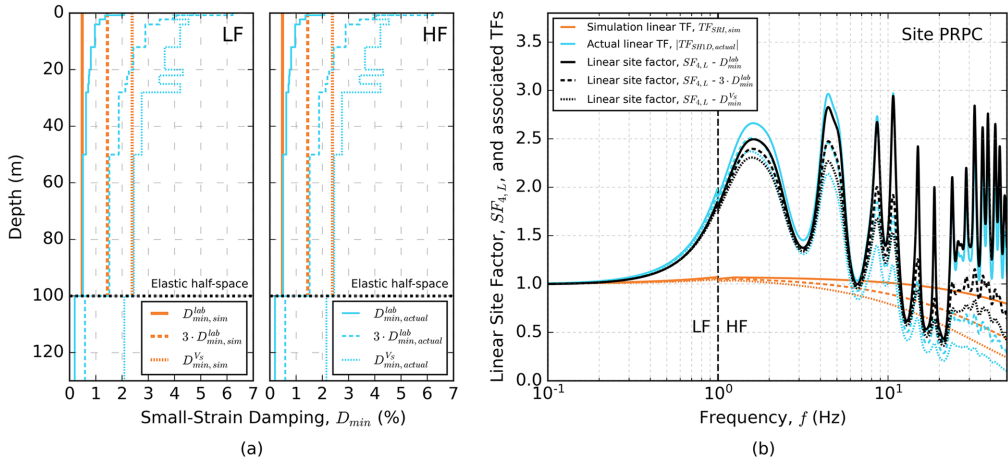


Figure 9. (a) D_{min} profiles used in Method 4 for the site PRPC. (b) Resulting linear site factor from Method 4 for the site PRPC.

borehole arrays in Japan and California. The 100-m depth considered in this article to perform the site adjustments is within the depth range considered by Pretell et al. (2023) to derive this multiplicative factor (sites with depths mostly less than 230 m); caution should be used for significantly deeper profiles. The Campbell (2009) $Q - V_S$ relationship adopted in (3) was selected based on its previous utilization in several site response studies (e.g. Afshari and Stewart, 2019; Cabas et al., 2017; Xu et al., 2020; Zhu et al., 2022). Some of them (e.g. Cabas et al., 2017; Xu et al., 2020) have found that this relationship better captures the field attenuation inferred from downhole array sites than the Darendeli (2001) model (D_{min}^{lab}). Given that for Method 4, it is assumed that the only site information available is the $V_{S,actual}$ profile, it is considered that the plasticity index (PI) is 0 for all layers, and the V_S -based correlation provided in Rix et al. (2019) is used for estimating ρ_{actual} .

In the case of Method 3, the parameter $\kappa_{0,sim}$ was used in the denominator of Equation 10 to remove the HF attenuation introduced by the full simulation site profile. In Method 4, $\Delta\kappa_{0,sim}$ is used in the denominator of Equation 13 instead, which only accounts for the portion of the site attenuation produced above the elastic half-space considered. Unlike $\kappa_{0,sim}$ in Method 3, $\Delta\kappa_{0,sim}$ is not a direct input parameter of the HF simulation, and hence, $\Delta\kappa_{0,sim}$ has to be estimated in Method 4. Under the assumption that this parameter represents additive attenuation effects over the simulation soil layers above the elastic half-space, $\Delta\kappa_{0,sim}$ can be expressed as (Cabas and Rodriguez-Marek, 2017):

$$\Delta\kappa_{0,sim} = \sum_{i=1}^n \frac{H_{sim,i}}{Q_{sim,i} V_{S,sim,i}} \quad (15)$$

where $H_{sim,i}$, $Q_{sim,i}$, and $V_{S,sim,i}$ are the thickness, quality factor, and shear-wave velocity of each layer i in the simulation profile, respectively, and the sum is performed over the n layers above the elastic half-space. Using $Q_{sim} = 1/(2D_{min,sim})$, Q_{sim} can be estimated via any of the three formulations considered for $D_{min,actual}$. For internal consistency, the same approach that is used for obtaining $D_{min,actual}$ is also used for estimating $D_{min,sim}$. In all the cases investigated in this study, $\Delta\kappa_{0,sim}$ is computed on the basis of a 100-m deep layer

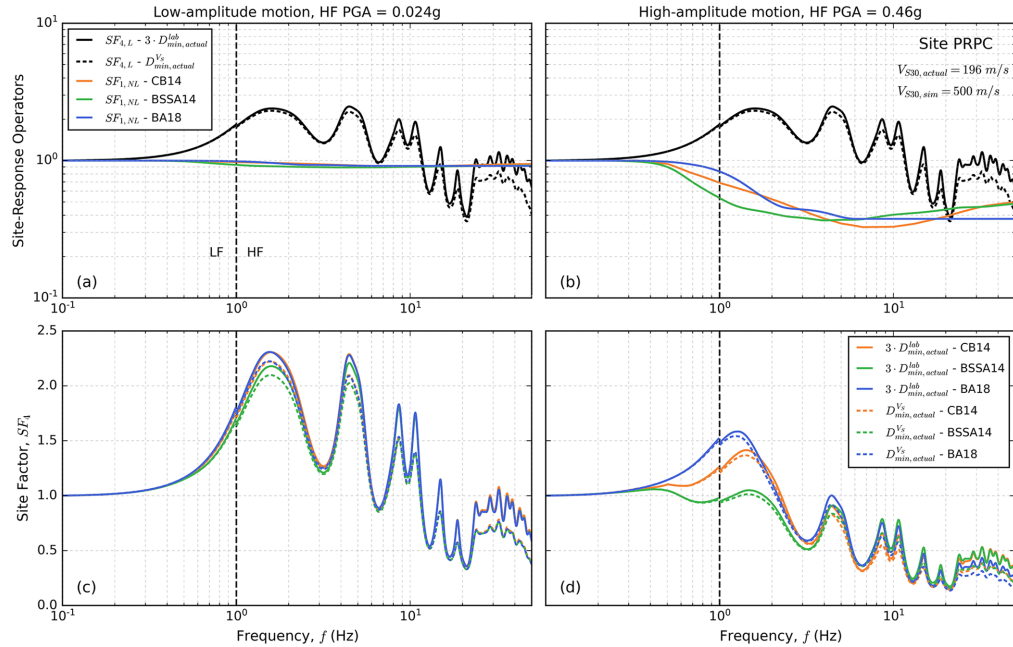


Figure 10. (a) Site-response operators of Method 4 for the site PRPC considering the low-amplitude motion, (b) the high-amplitude motion, (c) resulting site factors for the low-amplitude motion, and (d) high-amplitude motion.

with $V_{S,\text{sim}} = 500 \text{ m/s}$, which results in the following $\Delta\kappa_{0,\text{sim}}$ values for the damping formulations based on D_{\min}^{lab} , $3 \cdot D_{\min}^{\text{lab}}$, and $D_{\min,\text{actual}}^{V_S}$, respectively: 0.00192 s, 0.00576 s, and 0.00953 s.

Figure 9 illustrates the computation of the linear component of Method 4 for the site PRPC. Figure 9a shows the $D_{\min,\text{actual}}$ and $D_{\min,\text{sim}}$ profiles, and Figure 9b presents the resulting linear SFs ($SF_{4,L}$), along with the linear site response associated with the actual and simulation profiles. Figure 9a shows that the V_S -based damping formulation ($D_{\min,\text{actual}}^{V_S}$) generally results in a larger damping than $3 \cdot D_{\min,\text{actual}}^{\text{lab}}$ for the site PRPC. Figure 9b illustrates that the selection of the damping formulation has a greater impact at the peaks of the actual linear site response, and at very high frequencies ($f > 10 \text{ Hz}$).

Figure 10 shows the SFs (SF_4), along with the underlying operators, $SF_{4,L}$ and $SF_{1,NL}$, for the low-amplitude and high-amplitude motions, considering two alternative formulations for the computation of D_{\min} , and three alternative GMMs for the computation of $SF_{1,NL}$. D_{\min}^{lab} was excluded considering that the evidence suggests that $3 \cdot D_{\min}^{\text{lab}}$ or $D_{\min}^{V_S}$ provide more realistic values (e.g. Cabas et al., 2017; Pretell et al., 2023; Xu et al., 2020). Figures 10a and c illustrate that in the case of the low-amplitude motion, the selection of the damping formulation generally introduce a greater variability than the choice of the nonlinear model ($SF_{1,NL}$). On the other hand, Figures 10b and d show that for the high-amplitude motion, this sensitivity is frequency-dependent. In the frequency range $0.5 < f < 2 \text{ Hz}$, the selection of the nonlinear model is more relevant, whereas for $f > 25 \text{ Hz}$, the estimation of damping plays a more significant role.

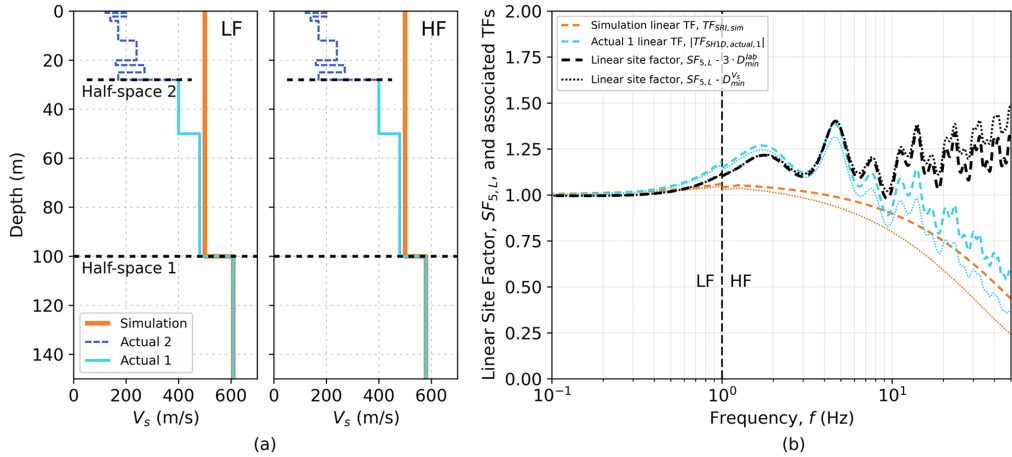


Figure 11. (a) V_s profiles used in Methods 5 for the site PRPC. (b) Resulting linear site factor.

Method 5—1D time-domain wave propagation analysis

Method 5 is a two-step procedure that generally requires more site-characterization data than Methods 3 and 4. Similar to Method 4, it relies on the SH1D assumptions but uses 1D time-domain wave propagation analysis (Approach B) to capture the near-surface nonlinear site response. In this method, the actual profile is divided into two portions: the “actual 1” and “actual 2” profiles. As illustrated in Figure 11a, for the site PRPC, the actual 2 profile corresponds to the shallower portion, which is bounded by a significant impedance contrast at the bottom (corresponding to the top of the Riccarton Gravel Formation, characterized by $V_s = 400$ m/s). As previously shown in Figure 2, the actual 2 profile is well characterized, with site-specific measures of V_s and CPT. On the other hand, the actual 1 profile is the deeper portion of the actual profile, for which soil nonlinearity can be assumed negligible. In the case of the site PRPC, location-specific site-characterization data are not available for this depth range.

Figure 12 illustrates Method 5. In Step 1, a linear SF, $SF_{5,L}$, is applied to the simulated ground motion (separately for the LF and HF components, as in the previous frequency-domain methods). This linear SF is obtained using the same equation used in Method 4 to compute $SF_{4,L}$ (Equation 13), but with the “actual 1” properties in the numerator (instead of the “actual” properties). $SF_{5,L}$ is computed relative to the half-space 1, shown in Figure 11a for the site PRPC. Figure 11b presents the resulting linear SF, for two different damping formulations, illustrating relatively small variability due to damping selection. The output of Step 1 is an outcrop broadband (BB) acceleration time series, $a_{input}(t)$, which is then used as input motion for the 1D time-domain nonlinear inelastic site-response analysis performed in Step 2. This analysis is conducted using the actual 2 profile and the half-space 2, illustrated in Figure 11a for the site PRPC.

The main reason for computing the site-response of the actual profile in two steps (i.e. using the actual 1 and 2 profiles) is to deal with different half-space 1 properties for the LF and HF components. In the case of the site PRPC, the difference between LF and HF V_s at half-space 1 is minor, but other sites (e.g. CMHS) may display significant deviations. 1D Time-domain site-response analysis requires a broadband input ground motion, and Step 1 allows for obtaining it at a common reference condition for LF and HF (half-space

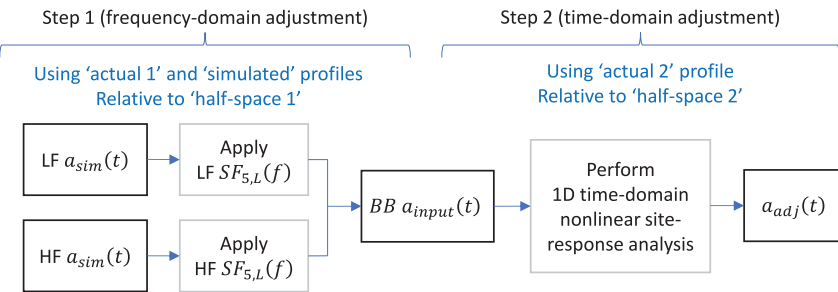


Figure 12. Illustration of Method 5. In Step 1, a frequency-domain adjustment is performed to the LF and HF simulated ground motions ($a_{sim}(t)$), which results in a BB ground motion ($a_{input}(t)$) used in Step 2; in Step 2, a 1D time-domain nonlinear inelastic site-response analysis is performed, which results in the adjusted acceleration time series, $a_{adj}(t)$, which accounts for shallow site effects.

2). This procedure also has the benefit of reducing the size of the site-response model for time-domain nonlinear analysis, limiting it to the depth range where soil nonlinearity is expected and where more site-characterization data are available to estimate site-response model parameters. However, decoupling the site-response analysis via this two-step procedure may introduce some errors in the site-response computation (Cabas et al., 2022), and hence, the selection of half-space 2 must be done with caution. Cabas et al. (2022) showed, for example, that a half-space located at a shallow impedance contrast mitigates this issue.

For the 1D time domain site-response analysis, different codes (Hashash et al., 2020; Jsh9, 2023; McKenna, 2011) and constitutive models (Groholski et al., 2016; Shi and Asimaki, 2017; Yang et al., 2003) were used to investigate the impact of alternative modeling decisions on the resulting site adjustment. The results of these analyses, summarized in the “Method 5” section of Electronic Supplement C, show that when the comparison is performed in a consistent manner (i.e. using the same modulus reduction (MR) curves), the variability in the site adjustment is significantly reduced. Therefore, in the following section, the results for Method 5 are only provided for the case in which the program OpenSees (McKenna, 2011) is used, along with the constitutive models PressureDependMultiYield02 and PressureIndependMultiYield (Yang et al., 2003, 2008), and user-defined MR curves. The MR curves were defined based on the Darendeli (2001) model, with a large-strain adjustment (Yee et al., 2013) for consistency with the soil shear strength. The estimation of the soil properties (e.g. actual soil density, PI, friction angle, and undrained shear strength) was based on the V_S profile, and the CPT, borehole, and SPT data available at each site, including the use of CPT-based correlations provided in Robertson and Cabal (2022). This resulted in the characterization of some soil properties (e.g. ρ_{actual}) with different values compared to those considered in Methods 3 and 4, where only the V_S profile was used as site information.

Comparison of the site amplification obtained with the five methods

Prior figures for each method focused on intra-method differences due to input parameter and model alternatives, using the site PRPC as an example. This section provides a comparison between the five methods for all four case study sites. Figure 13 presents a comparison of the linear SFs (SF_L) obtained with Methods 1–4. Given that the treatment of the nonlinear component of the SFs (SF_{NL}) is the same for these four methods, only the linear

component is compared in this figure, but the effect of soil nonlinearity in the resulting AFs is examined subsequently. Two alternative GMMs (CB14 and BA18) are considered for Method 1 (V_{S30} -based amplification), and the CB14 model is considered for Method 2 (V_{S30} -based amplification with host-to-target adjustment). The CB14 is considered because it has been used in several previous studies (e.g. Lee et al., 2022; Razafindrakoto et al., 2018), and the BA18 model is included to illustrate the differences between SA- and FAS-based models. Also, two different estimates of $\kappa_{0,actual}$ and $D_{min,actual}$ are examined for Method 3 (SRI-based amplification) and Method 4 (1D TF-based amplification), respectively. For each site, the predominant frequency of the near-surface soil profile, f_{site} , is plotted, which is estimated based on the lowest frequency peak in $SF_{4,L}$.

Figure 13 shows that in the four sites investigated, the linear SFs obtained with Methods 3 and 4 mainly affect the HF range and tend to a value of 1 at low frequencies, reflecting the fact that the adjustment is only accounting for shallow site effects (within the top 100 m); whereas Methods 1 and 2 generally produce considerable amplification in the LF range. Following this, and considering that the compatibility with the regional-scale simulation is explicitly controlled in Methods 3 and 4, in the case of Methods 1 and 2, the SF is only applied to the HF simulation component (such as in Lee et al., 2022). The implementation of this procedure is described in Electronic Supplement B. Figure 13 suggests that the frequency range of application of these SFs should be defined in a site-specific manner, but for Methods 1 and 2, it is assumed that a site-specific V_S profile is not available.

In the case of the four sites considered, Method 1 produces higher amplification than Methods 3 and 4 in the vicinity of $f = 1$ Hz, reflecting the previously discussed limitations of this approach. Method 2, which better accounts for the compatibility with the regional ground-motion simulation, reduces this relative overamplification, particularly in the frequency range $1 < f < 2$ Hz, but generally does not eliminate it.

The ergodic assumption implicit in Method 1 is illustrated when comparing the linear SFs for the sites PRPC and CMHS. These two sites are characterized by very similar V_{S30} values, resulting in almost identical SF_L produced by Methods 1 with the CB14 model (which only depends on V_{S30}). Methods 3 and 4, on the other hand, produce significantly different linear site amplification at these two sites, reflecting the differences in the site-specific V_S profiles (see Figure 2), which are accounted for by these methods.

Method 4 produces significant variations in the SFs over narrow frequency bands, whereas Method 3 results in SFs varying smoothly with frequency. In particular, Method 4 generates significantly greater amplification than Method 3 around f_{site} in all four sites considered and, in some cases, also around higher frequencies, which is driven by resonance effects not modeled by Method 3.

Figure 13 illustrates that the definition of $\kappa_{0,actual}$ in Method 3 can have a considerable impact on the resulting linear SFs at high frequencies. This is particularly true in the case of the sites RHSC and CACS, which are characterized by relatively high $V_{S30,actual}$ values, resulting in lower estimates of $\kappa_{0,actual}$. The $V_{S30} - \kappa_0$ correlation of Bayless and Abrahamson (2019) in these cases results in a $\kappa_{0,actual}$ (i.e. $\kappa_{0,actual(BA19)}$) that is lower than the constant value $\kappa_{0,sim} = 0.045$ s used in the regional ground-motion simulations. This negative $\Delta\kappa_0 = (\kappa_{0,actual} - \kappa_{0,sim})$ value (-0.001 s for RHSC and -0.007 s for CACS) produces HF amplification instead of attenuation, which explains the big differences observed at very high frequencies when comparing the SF_L obtained using $\kappa_{0,actual(BA19)}$ and $\kappa_{0,actual(X20)}$. The reason why the impact of $\kappa_{0,actual}$ is significant in Method 3, compared to

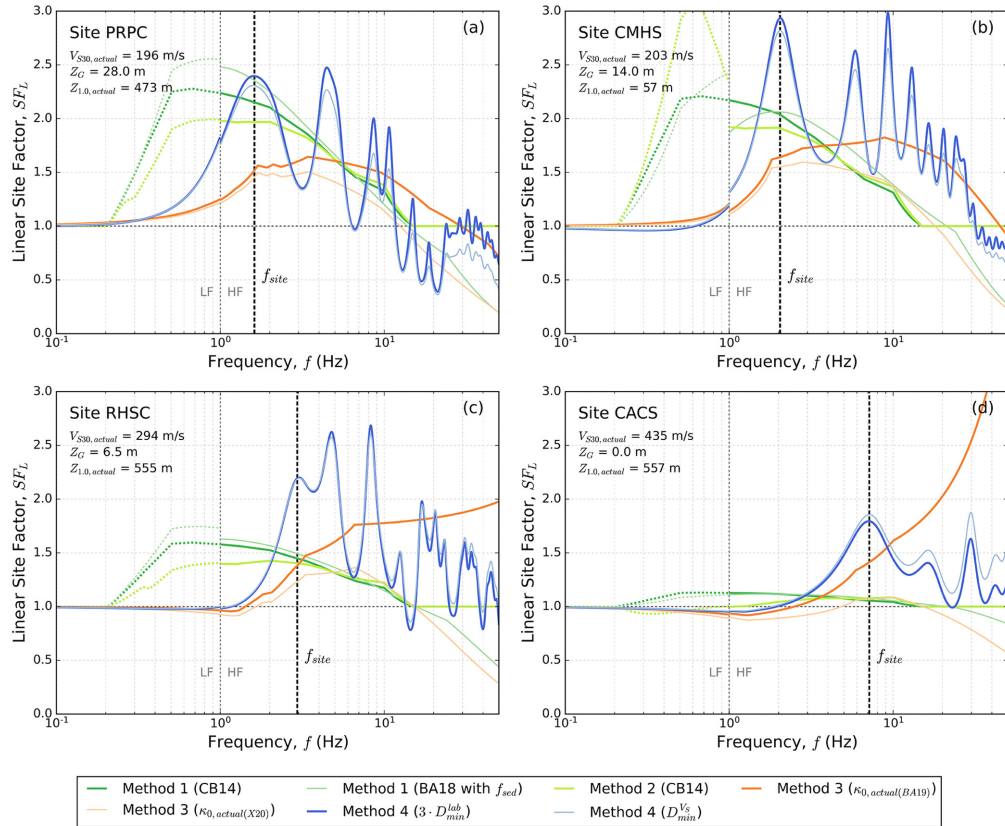


Figure 13. Comparison of the linear factors obtained with Methods 1–4 for the sites: (a) PRPC, (b) CMHS, (c) RHSC, and (d) CACS. Dashed lines in Methods 1 and 2 indicate that the LF component is not used in the adjustment.

the role that $D_{min,actual}$ has on Method 4 (as clearly observed in Figure 13d), is that the parameter $\kappa_{0,actual}$ accounts for cumulative effects of damping over the full site profile. In this way, $\Delta\kappa_0$ can be accounting for differences produced by layers much deeper than 100 m, whereas $D_{min,actual}$ only acts in the shallow portion of the site profile. An alternative implementation of Method 3 that accounts for attenuation in a manner analogous to Method 4 is possible, but the current implementation was considered because of the convenience of using $\kappa_{0,sim}$ and $\kappa_{0,actual}$ as input parameters: $\kappa_{0,sim}$ is a direct input parameter (i.e. known value) of the regional ground-motion simulation, and there is a growing interest in the development of methods and models for estimating κ_0 at a given site (i.e. $\kappa_{0,actual}$) (e.g. Ktenidou et al., 2014; Xu et al., 2020).

Figures 14 and 15 present the AFs, which now include the influence of nonlinearity, that result from applying Methods 1–5 to the four sites investigated, for the low- and high-amplitude ground motion, respectively. For a given IM, AF is defined as

$$AF = \frac{IM_{adj}}{IM_{sim}} \quad (16)$$

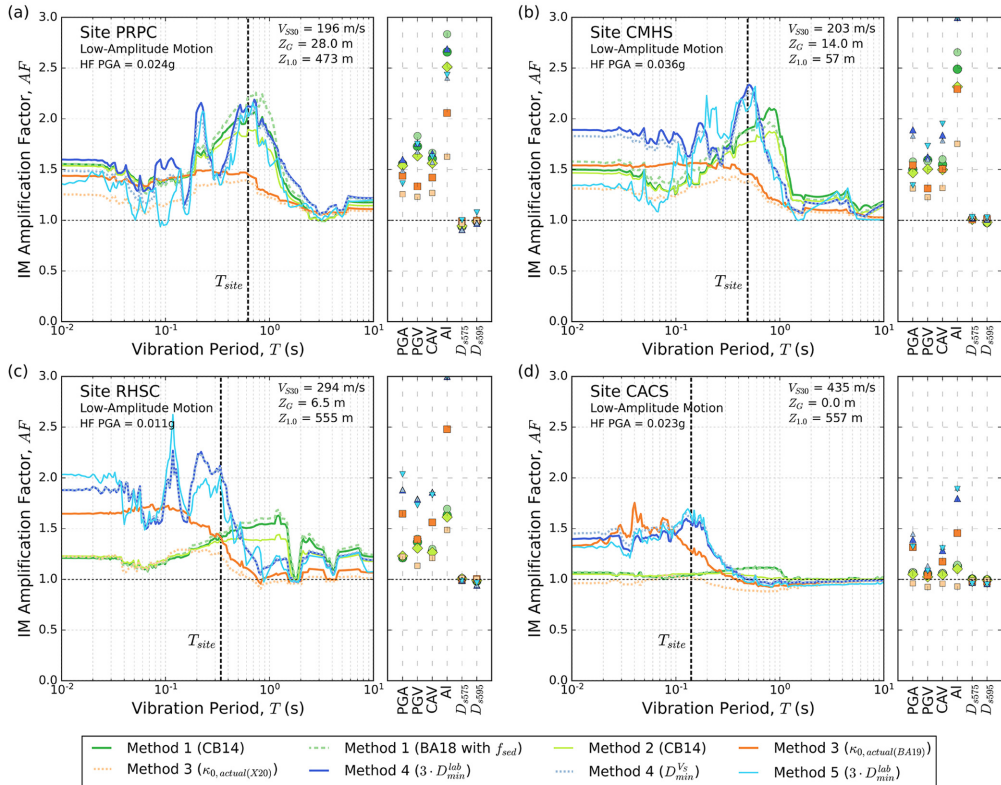


Figure 14. Amplification factors of different IMs resulting from applying Methods 1–5 to the sites: (a) PRPC, (b) CMHS, (c) RHSC, and (d) CACS, for the low-amplitude ground motion. For visual completeness, the AI AFs for the sites CMHS and RHSC associated with Methods 4 and 5 are plotted at the vertical axis limit (3.0). The actual values for CMHS are 3.45 (Method 4 using $3 \cdot D_{min}^{lab}$), 3.25 (Method 4 using $D_{min, actual}^{V_s}$), and 3.49 (Method 5); and for RHSC, the actual values are 3.64 (Method 4 using $3 \cdot D_{min}^{lab}$), 3.64 (Method 4 using $D_{min, actual}^{V_s}$), and 3.53 (Method 5).

where IM_{adj} is the IM for the adjusted ground motion, and IM_{sim} is the IM for the simulated (unadjusted) ground motion. The IMs considered are SA for vibration periods between $T = 0.01\text{--}10$ s, PGA, peak ground velocity (PGV), cumulative absolute velocity (CAV), Arias intensity (AI), and the 5%–75% and 5%–95% significant duration (D_{s575} and D_{s595} , respectively). In the case of Methods 1–4, the same models and inputs used in Figure 13 are considered. For Methods 3 and 4, the nonlinear operator derived from the BA18 model is used, and for Method 5, only the OpenSees analysis using user-defined MR curves is examined. Figures 14 and 15 include the predominant period of the near-surface soil profile, estimated as $T_{site} = 1/f_{site}$

In the case of the low-amplitude motion (Figure 14), which produces relatively low levels of soil nonlinearity, the response spectral amplification generally follows a shape and amplitude similar to the linear SFs plotted in Figure 13 in the intermediate period range (approximately $0.1 < T < 1$ s). However, at shorter and longer vibration periods, this is not the case. For example, there are several cases in Figure 13 where the linear SF produces de-amplification at high frequencies, but this de-amplification is not observed in AF

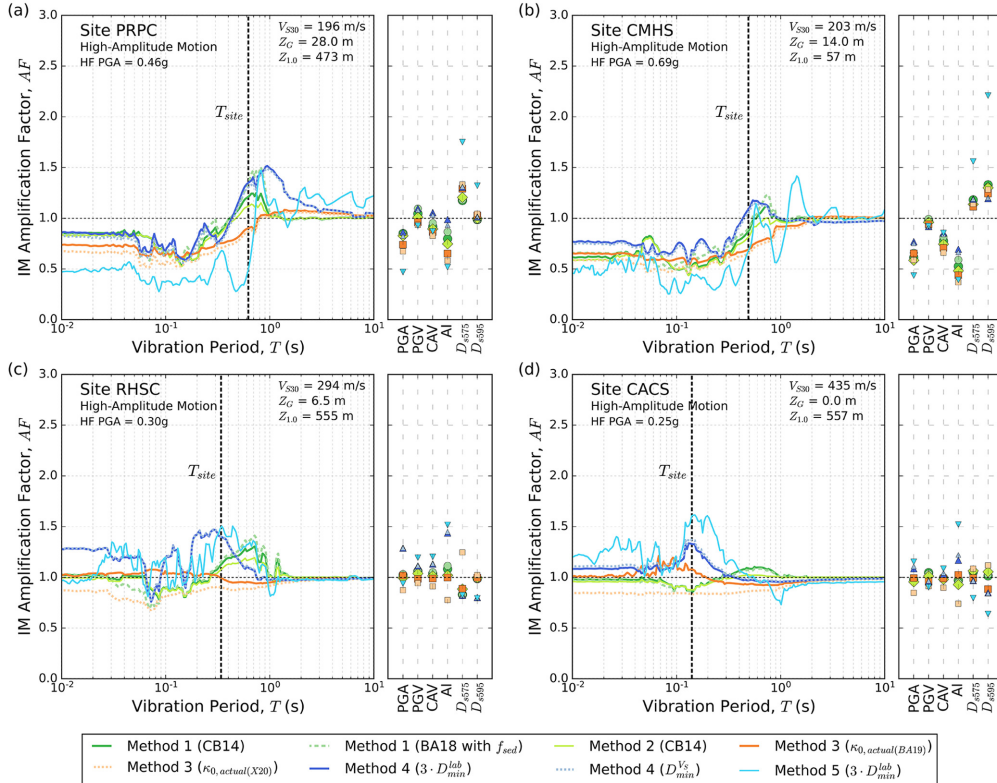


Figure 15. Amplification factors of different IMs resulting from applying Methods 1–5 to the sites: (a) PRPC, (b) CMHS, (c) RHSC, and (d) CACS, for the high-amplitude ground motion.

(Figure 14) at short vibration periods, which is due to the difference between FAS and SA (Bora et al., 2016). At low frequencies, all the linear SFs tend to $SF_L = 1$ in Figure 13, whereas in Figure 14, $AF > 1$ values are observed at very long vibration periods. However, these periods are associated with relatively low SA values, and therefore, these $AFs > 1$ do not imply a noticeable increment in SA in absolute terms. These trends can be observed more clearly in the “Comparison between methods” section of Electronic Supplement C, where AF and SA are shown superimposed, for the two ground-motion intensity levels considered. Furthermore, Figure 14 illustrates that (1) the reduction in amplification produced by Method 2 relative to Method 1 in the SF domain (which mainly occurs in the intermediate frequency range) is also produced in the AF domain (for SA); and (2) the significant differences observed in the SFs at high frequencies between the CB14 and BA18 models in Method 1, and between the two estimates of $\kappa_0, actual$ in Method 3, are reduced considerably in the case of AF.

Figure 14 also shows that Method 4 and 5 generally display similar shapes and amplitudes in the response spectral AF for the low-amplitude motions, which is expected given that both methods rely on 1D site-response analysis. However, at some vibration periods, considerable differences are observed due to the different treatment of nonlinear site-response, the use of more site-specific data, and the decoupling of the site-response analysis in Method 5. For example, for the site CMHS, at very short vibration periods, Method

5 results in considerably lower values of amplification. This is mainly due to the more significant soil nonlinearity predicted by Method 5, which is modeled in a site-specific fashion, accounting for the relatively low values of cone resistance at this site (see Figure 2).

AI displays particularly high levels of amplification and method-to-method variability in Figure 14, especially in the case of the softer sites. On the other hand, the significant durations D_{s575} and D_{s595} are almost not influenced by the shallow site-response adjustments under the low-amplitude motions.

Figure 15 shows that for the high-amplitude motion considered, soil nonlinearity has a strong influence on AF, especially for the softer sites, PRPC, and CMHS. At these sites, severe de-amplification is observed at short-period SAs, PGA, and AI, and amplification is generally produced in the significant durations D_{s575} and D_{s595} . Figure 15 also illustrates the difference between an ergodic treatment of soil nonlinearity based on V_{S30} (Methods 1–4) and a site-specific treatment as in Method 5. In the case of PRPC and CMHS, Method 5 generally resulted in stronger de-amplification at short vibration periods, and it was able to capture the softening of the soil deposits, manifested in the shift of the maximum response spectral AFs toward longer vibration periods, whereas the ergodic approach simply results in general reduction and smoothing of the linear amplification. This produces considerable differences in AF over certain period ranges between Methods 4 and 5 (e.g. between 1 and 2 s at CMHS). Also, Method 5 produces more significant amplification of D_{s575} and D_{s595} in these sites.

Discussion

Table 4 summarizes the main advantages and disadvantages of the five methods investigated and illustrates important trade-offs between them. Going from Method 1 to Method 5 involves the use of increasing levels of site-characterization data and more location-specific treatment of the site adjustment.

Other than the simplicity and small requirement of site information (which is ideal for regional applications), the only conceptual advantage of Methods 1 and 2 is their ability, via empirical calibration, to implicitly capture complex phenomena observed in reality that are difficult to explicitly model using physics-based methods. It is worth noting that although Methods 3–5 make use of physics-based approaches and additional site-specific data, these approaches are limited to the use of a 1D representation of the soil profile, and hence, they are unable to explicitly model 3D effects. However, the actual characteristics of these 3D effects are region- and site-specific, which may limit the ability of Methods 1 and 2 to offer a significant advantage, especially in regions other than those for which the empirical models were calibrated. Another related situation where Method 1 can produce beneficial effects is when it compensates for unmodeled phenomena in the regional-scale simulation. For example, although the LF simulation in the GP method explicitly models 3D effects, its ability to properly capture them strongly depends on the quality of the velocity model considered. Method 1 implicitly captures site effects associated with the deep velocity structure of a site (e.g. basin effects and impedance-based amplification associated with deep layers), which can result in strong amplification at relatively low frequencies when compared with the other methods, especially for sites with low $V_{S30,actual}$ values. If the 3D velocity structure is well modeled in the LF simulation, this should lead to overamplification due to double-counting deep velocity structure effects, which has been speculated to have been present in previous validation studies (e.g. de la Torre et al., 2020; Lee et al., 2020, 2022). However, if the 3D velocity model utilized in the LF simulation is

Table 4. Comparison between five methods investigated

Method	Concept	Pros	Cons
1	V_{S30} -based amplification	Only requires the V_{S30} site proxy (and in some cases, $Z_{1.0}$ or $Z_{2.5}$) Easier implementation than Methods 2–5 Suitable for regional applications Can capture complex phenomena evident in observations but not well modeled by conventional physics-based methods	Can produce significant overamplification at relatively low frequencies, particularly for soft soil sites Ergodic treatment of linear and nonlinear site response
2	V_{S30} -based amplification with host-to-target adjustment	All the pros of Method 1 Compatibility with regional-scale ground motion simulation is improved, reducing overamplification issues produced by Method 1	GMM host profile can be difficult to obtain Ergodic treatment of linear and nonlinear site response
3	SRI-based amplification; combined with the nonlinear component of Method 1	Site-specific treatment of linear site response Based on a V_S profile Compatibility with regional-scale ground-motion simulation is explicitly controlled Not sensitive to details in the V_S profile and the associated uncertainty	Only models 1D impedance effects, ignoring resonance phenomena Ergodic treatment of nonlinear site response
4	1D transfer function-based amplification; combined with the nonlinear component of Method 1	Site-specific treatment of linear site response Based on a V_S profile Compatibility with regional-scale ground-motion simulation is explicitly controlled Can model resonance effects, which are not modeled in Method 3	Performance notably diminishes when the 1D wave-propagation assumption does not hold, and resonance effects can be excessive in the transfer function if the V_S profile is too simple, with large impedance contrasts that are not physically present Ergodic treatment of nonlinear site response
5	1D time-domain nonlinear inelastic wave propagation analysis	Site-specific treatment of linear and nonlinear site response Compatibility with regional-scale simulation is explicitly controlled	Performance diminishes when the 1D wave-propagation assumption does not hold Generally requires more site-characterization data than Methods 1–4, and greater expertise to calibrate the constitutive models and perform the analysis

deficient, such that the predicted LF amplification is less than actual, this “subtractive cancellation” may result in lower residuals at low frequencies when using Method 1.

Method 2 partially deals with the host-to-target adjustment issue present in Method 1 and can reduce the Method 1 overamplification in both the LF and HF range. However, the resulting amplification in the LF range may still be significantly higher than that obtained from Methods 3–5 for relatively soft sites. This limited effect of Method 2 on low frequencies may be due to basin effects implicit in the GMM, which are not removed by this method; challenges associated with the determination of an accurate 1D host profile, required in Method 2; and limitations of the SRI method, which is used to compute the reference correction factor.

Methods 3–5 explicitly control the compatibility with the regional-scale simulation. The effects produced by the simulation in the shallow portion of the site are removed and modified in a site-specific manner, which avoids the host-to-target adjustment issue present in Method 1, and to a lesser extent, Method 2. Also, in contrast to Methods 1 and 2, these methods explicitly model the site-response physics to different extents using a 1D representation of the site. Therefore, the suitability of this representation, along with the quality of the site-characterization data, will determine the performance of these methods, especially in the case of Methods 4 and 5 which more strongly rely on the SH1D assumptions. Evidence suggests that these assumptions may only hold for a modest percentage of cases (e.g. Afshari and Stewart, 2019; Thompson et al., 2012), and even for such “1D” sites, 1D site-response analysis can be inaccurate (Pretell et al., 2023). Because of this, several approaches have been proposed to adjust 1D site-response analysis to implicitly account for spatial variability and other unmodeled phenomena (e.g. Hallal et al., 2022; Pretell et al., 2023). However, their capacity to improve predictions is generally limited to 1D-like sites. Thus, advancing the use of a time-domain adjustment with 2D or 3D site-response analysis (e.g. de la Torre et al., 2022a, 2022b; Hallal and Cox, 2021) may be required to significantly improve predictions at complex sites, which would involve the collection of further site-characterization data, and to properly address the compatibility issue between the regional simulation and the 2D/3D site-response model.

The aforementioned discussion illustrates that it is not possible to determine *a priori* the best method to adjust hybrid broadband ground-motion simulations. The quality of the regional velocity model; characteristics of the site and its location within the sedimentary basin and relative to earthquake source (e.g. Smerzini et al., 2011); and site-characterization data available will dictate which method is the most appropriate to use. This highlights the need for systematic validation of alternative methods against observations (e.g. Kuncar et al., 2024) to inform method and model selection in forward applications.

Conclusions

This article presented a comprehensive examination on the incorporation of shallow site effects in hybrid broadband ground-motion simulations. Five methods were presented that allow for the adjustment of ground-motion time series produced by regional simulations to account for unmodeled site effects and represent a wide range of options in terms of the site-characterization data and expertise required. The methods were applied to four sites representative of different soil conditions, and two levels of ground-motion amplitude were considered, to investigate the relative adjustment that they can generate on different IMs.

The results show that significant variability exists in the SFs and IM amplifications predicted by the different methods. Method 1 (V_{S30} -based amplification) has been commonly adopted because of its simplicity and low requirement of site information, but some validation studies have recently shown that its application may produce systematic overprediction at relatively long vibration periods. This article provided an explanation for this systematic feature, which is related to the incompatibility between the V_S profile implicit in the regional ground-motion simulation and the corresponding profile implicit in the GMM used in Method 1 for the same V_{S30} value, in addition to the potential double-counting of deep 3D velocity structure effects. Based on this, different strategies were discussed to mitigate this issue: (1) applying the SF to the HF simulation component only; (2) including the f_{sed} term in the case of models that allow for a V_{S30} -based f_{sed} correction; and (3) using Method 2, which requires the same site information as Method 1 but involves the application of a host-to-target V_S adjustment. The application of this method to the four sites considered showed that it allows for a reduction in the relative overamplification of Method 1, both in the Fourier and response spectral domain, but only to a limited degree. Given these limitations, Methods 1 and 2 have to be used with caution, especially in the case of soft sites where this issue is more prominent.

Methods 3 and 4 were proposed as alternatives when a V_S profile is available at the site, but the site-characterization data are not sufficient to constrain advanced nonlinear site-response analyses. The study showed that the SFs derived by these two methods can present significant differences, and further research is needed to understand which one produces better predictions under specific conditions. Comparison between Methods 4 (which uses a V_{S30} -based approach to capture soil nonlinearity) and the more advanced Method 5, based on 1D time-domain nonlinear site-response analysis, generally showed similar SA amplifications under low-amplitude motions, but significant differences were observed at some sites and period ranges, under low- and high-amplitude motions. These results suggest that for sites that significantly depart from the average conditions considered in V_{S30} -based nonlinear models (e.g. sites likely to exhibit large shear strains over a small depth range in the deposit as a result of large impedance contrasts and/or particularly weak materials), Method 5 may result in improved ground-motion predictions.

Several sources of parametric and modeling uncertainty are involved in each method, which can produce considerable within-method variability as shown by the sensitivity analyses performed in this study. In particular, the definition of $\kappa_{0,actual}$ in Method 3 can have a strong influence in the resulting SF at high frequencies, especially in the case of relatively stiff sites, although this impact decreases in the response spectral domain. Here, generic V_{S30} -based correlations were used to estimate $\kappa_{0,actual}$, but this parameter can be better constrained by developing region-specific maps or correlations, or directly estimating it from ground-motion recordings.

Advances in computational capability, theory, and knowledge will allow for explicitly modeling shallow site effects in 3D numerical simulations, but this progress will be region-specific. In the interim, the methods presented in this article can be used in engineering applications, and this study can help to clarify their limitations and the impact of different modeling decisions. To evaluate the relative performance of these methods under a diverse range of earthquake sources, site conditions, and site-characterization data, direct comparison with observations from multiple sites and events is needed.

Acknowledgments

The authors thank Linda Al Atik for providing the host profiles that were used to illustrate the application of Method 2, and Sean Ahdi and two anonymous reviewers for providing valuable comments on the manuscript. The authors would also like to gratefully acknowledge the New Zealand eScience Infrastructure (NeSI) and the Korea Institute of Science and Technology Information (KISTI) [KSC-2023-CRE-0459] for the high-performance computing resources provided.

Declaration of conflicting interests

The author(s) declared no potential conflicts of interest with respect to the research, authorship, and/or publication of this article.

Funding

The author(s) disclosed receipt of the following financial support for the research, authorship, and/or publication of this article: This work was financially supported by the University of Canterbury, QuakeCoRE: The NZ Center for Earthquake Resilience, Resilience to Nature's Challenges National Science Challenge, the Marsden Fund, and the New Zealand Natural Hazards Commission (Toka Tū Ake). This is QuakeCoRE publication number 978.

ORCID iDs

Felipe Kuncar  <https://orcid.org/0000-0003-2779-2290>

Brendon A Bradley  <https://orcid.org/0000-0002-4450-314X>

Christopher A de la Torre  <https://orcid.org/0000-0002-7946-7812>

Adrian Rodriguez-Marek  <https://orcid.org/0000-0002-8384-4721>

Chuanbin Zhu  <https://orcid.org/0000-0001-8097-2237>

Robin L Lee  <https://orcid.org/0000-0003-1033-5923>

Data and resources

Figures 1, 5, and 12 were prepared using Microsoft PowerPoint, and the remaining figures were generated in Python (<https://www.python.org/>). The host profiles derived by Linda Al Atik (personal communication, April 6, 2023), that were used to illustrate the application of Method 2, are provided in the Supplemental Material. The New Zealand Velocity Model (NZVM) code is available at <https://github.com/ucgmsim/Velocity-Model>.

Supplemental material

Supplemental material for this article is available online.

References

- Afshari K and Stewart JP (2019) Insights from California vertical arrays on the effectiveness of ground response analysis with alternative damping models. *Bulletin of the Seismological Society of America* 109(4): 1250–1264.
- Al Atik L and Abrahamson N (2021) A Methodology for the development of 1D reference vs profiles compatible with ground-motion prediction equations: Application to NGA-West2 GMPEs. *Bulletin of the Seismological Society of America* 111(4): 1765–1783.
- Anderson JG and Hough SE (1984) A model for the shape of the Fourier amplitude spectrum of acceleration at high frequencies. *Bulletin of the Seismological Society of America* 74(5): 1969–1993.
- Ayoubi P, Mohammadi K and Asimaki D (2021) A systematic analysis of basin effects on surface ground motion. *Soil Dynamics and Earthquake Engineering* 141: 106490.

- Baker J, Bradley B and Stafford P (2021) *Seismic Hazard and Risk Analysis*. Cambridge: Cambridge University Press.
- Bard PY, Bora SS, Hollender F, Laurendeau A and Traversa P (2020) Are the standard vs-kappa host-to-target adjustments the Only way to get consistent hard-rock ground motion prediction? *Pure and Applied Geophysics* 177(5): 2049–2068.
- Bayless J and Abrahamson NA (2019) Summary of the BA18 ground-motion model for Fourier amplitude spectra for crustal earthquakes in California. *Bulletin of the Seismological Society of America* 109(5): 2088–2105.
- Bielak J (2003) Domain reduction method for three-dimensional earthquake modeling in localized regions, part I: Theory. *Bulletin of the Seismological Society of America* 93(2): 817–824.
- Boore DM (2003) Simulation of ground motion using the stochastic method. *Pure and Applied Geophysics* 160(3): 635–676.
- Boore DM (2013) The uses and limitations of the square-root-impedance method for computing site amplification. *Bulletin of the Seismological Society of America* 103(4): 2356–2368.
- Boore DM and Abrahamson NA (2023) On the ratio of full-resonance to square-root-impedance amplifications for shear-wave velocity profiles that are a continuous function of depth. *Bulletin of the Seismological Society of America* 113: 1192–1207.
- Boore DM, Stewart JP, Seyhan E and Atkinson GM (2014) NGA-West2 equations for predicting PGA, PGV, and 5% damped PSA for shallow crustal earthquakes. *Earthquake Spectra* 30(3): 1057–1085.
- Boore DM, Thompson EM and Cadet H (2011) Regional correlations of VS30 and velocities averaged over depths less than and greater than 30 meters. *Bulletin of the Seismological Society of America* 101(6): 3046–3059.
- Bora SS, Cotton F and Scherbaum F (2019) NGA-West2 empirical Fourier and duration models to generate adjustable response spectra. *Earthquake Spectra* 35(1): 61–93.
- Bora SS, Scherbaum F, Kuehn N and Stafford P (2016) On the relationship between Fourier and response spectra: Implications for the adjustment of empirical ground-motion prediction equations (GMPEs). *Bulletin of the Seismological Society of America* 106(3): 1235–1253.
- Cabas A and Rodriguez-Marek A (2017) Vs- κ_0 correction factors for input ground motions used in seismic site response analyses. *Earthquake Spectra* 33(3): 917–941.
- Cabas A, Rodriguez-Marek A and Bonilla LF (2017) Estimation of site-specific kappa (κ_0)-consistent damping values at KiK-net sites to assess the discrepancy between laboratory-based damping models and observed attenuation (of seismic waves) in the field. *Bulletin of the Seismological Society of America* 107(5): 2258–2271.
- Cabas A, Rodriguez-Marek A, Green RA and Ji C (2022) Quantifying the error associated with the elastic halfspace assumption in site response analysis. *Journal of Geotechnical and Geoenvironmental Engineering* 148(10): 04022081.
- Campbell KW (2003) Prediction of strong ground motion using the hybrid empirical method and its use in the development of ground-motion (attenuation) relations in Eastern North America. *Bulletin of the Seismological Society of America* 93(3): 1012–1033.
- Campbell KW (2009) Estimates of shear-wave Q and κ_0 for unconsolidated and semiconsolidated sediments in Eastern North America. *Bulletin of the Seismological Society of America* 99(4): 2365–2392.
- Campbell KW and Bozorgnia Y (2008) NGA ground motion model for the geometric mean horizontal component of PGA, PGV, PGD and 5% damped linear elastic response spectra for periods ranging from 0.01 to 10_S. *Earthquake Spectra* 24(1): 139–171.
- Campbell KW and Bozorgnia Y (2014) NGA-West2 ground motion model for the average horizontal components of PGA, PGV, and 5% damped linear acceleration response spectra. *Earthquake Spectra* 30(3): 1087–1115.
- Darendeli MB (2001) *Development of a new family of normalized modulus reduction and material damping curves*. PhD Thesis, University of Texas at Austin, Austin, TX.
- de la Torre CA, Bradley BA and Lee RL (2020) Modeling nonlinear site effects in physics-based ground motion simulations of the 2010–2011 Canterbury earthquake sequence. *Earthquake Spectra* 36(2): 856–879.

- de la Torre CA, Bradley BA and McGann CR (2022a) 2D Geotechnical site-response analysis including soil heterogeneity and wave scattering. *Earthquake Spectra* 38(2): 1124–1147.
- de la Torre CA, Bradley BA, Stewart JP and McGann CR (2022b) Can modeling soil heterogeneity in 2D site response analyses improve predictions at vertical array sites? *Earthquake Spectra* 38(4): 2451–2478.
- Dreger DS, Beroza GC, Day SM, Goulet CA, Jordan TH, Spudich PA and Stewart JP (2015) Validation of the SCEC broadband platform V14.3 simulation methods using pseudospectral acceleration data. *Seismological Research Letters* 86(1): 39–47.
- Dupros F, De Martin F, Foerster E, Komatitsch D and Roman J (2010) High-performance finite-element simulations of seismic wave propagation in three-dimensional nonlinear inelastic geological media. *Parallel Computing* 36(5–6): 308–325.
- Evangelista L, del Gaudio S, Smerzini C, d'Onofrio A, Festa G, Iervolino I, Landolfi L, Paolucci R, Santo A and Silvestri F (2017) Physics-based seismic input for engineering applications: A case study in the Aterno river valley, Central Italy. *Bulletin of Earthquake Engineering* 15(7): 2645–2671.
- Fu H, He C, Chen B, Yin Z, Zhang Z, Zhang W, Zhang T, Xue W, Liu W, Yin W, Yang G and Chen X (2017) 18.9-Pflops nonlinear earthquake simulation on Sunway TaihuLight: Enabling depiction of 18-Hz and 8-meter scenarios. In: *Proceedings of the international conference for high performance computing, networking, storage and analysis*, Denver, CO, 12–17 November, pp. 1–12. New York: ACM.
- Graves R and Pitarka A (2015) Refinements to the Graves and Pitarka (2010) broadband ground-motion simulation method. *Seismological Research Letters* 86(1): 75–80.
- Graves R and Pitarka A (2016) Kinematic ground-motion simulations on rough faults including effects of 3D stochastic velocity perturbations. *Bulletin of the Seismological Society of America* 106(5): 2136–2153.
- Graves RW and Pitarka A (2010) Broadband ground-motion simulation using a hybrid approach. *Bulletin of the Seismological Society of America* 100(5A): 2095–2123.
- Groholski DR, Hashash YMA, Kim B, Musgrove M, Harmon J and Stewart JP (2016) Simplified model for small-strain nonlinearity and strength in 1D seismic site response analysis. *Journal of Geotechnical and Geoenvironmental Engineering* 142(9): 04016042.
- Hallal MM and Cox BR (2021) An H/V geostatistical approach for building pseudo-3D Vs models to account for spatial variability in ground response analyses part I: Model development. *Earthquake Spectra* 37(3): 2013–2040.
- Hallal MM and Cox BR (2023) What spatial area influences seismic site response: Insights gained from multiazimuthal 2D ground response analyses at the treasure Island Downhole Array. *Journal of Geotechnical and Geoenvironmental Engineering* 149(1): 04022124.
- Hallal MM, Cox BR and Vantassel JP (2022) Comparison of state-of-the-art approaches used to account for spatial variability in 1D ground response analyses. *Journal of Geotechnical and Geoenvironmental Engineering* 148(5): 04022019.
- Hartzell S (2002) Simulation of broadband ground motion including nonlinear soil effects for a magnitude 6.5 earthquake on the Seattle Fault, Seattle, Washington. *Bulletin of the Seismological Society of America* 92(2): 831–853.
- Hartzell S, Harmsen S, Frankel A and Larsen S (1999) Calculation of broadband time histories of ground motion: Comparison of methods and validation using strong-ground motion from the 1994 Northridge earthquake. *Bulletin of the Seismological Society of America* 89(6): 1484–1504.
- Hashash YMA, Harmon J, Ilhan O, Stewart JP, Rathje EM, Campbell KW, Silva WJ and Goulet CA (2018) Modelling of site amplification via large scale nonlinear simulations with applications to North America. In: Brandenberg SJ and Manzari MT (eds) *Geotechnical Earthquake Engineering and Soil Dynamics V*. Austin, TX: American Society of Civil Engineers, pp. 523–537.
- Hashash YMA, Musgrove MI, Harmon JA, Ilhan O, Xing G, Numanoğlu O, Groholski DR, Phillips CA and Park D (2020) DEEPSOIL 7.0. User Manual. Urbana, IL, Board of Trustees of University of Illinois at Urbana-Champaign. <https://deepsoil.cee.illinois.edu/>
- Haskell NA (1953) The dispersion of surface waves on multilayered media. *Bulletin of the Seismological Society of America* 43(1): 17–34.

- Joyner WB, Warrick RE and Fumal TE (1981) The effect of quaternary alluvium on strong ground motion in the Coyote Lake, California, earthquake of 1979. *Bulletin of the Seismological Society of America* 71(4): 1333–1349.
- Jsh9 (2023) Jsh9/PySeismoSoil: v0.5.3. DOI: 10.5281/ZENODO.7813062.
- Kaklamanos J, Bradley BA, Thompson EM and Baise LG (2013) Critical parameters affecting bias and variability in site-response analyses using KiK-net Downhole Array data. *Bulletin of the Seismological Society of America* 103(3): 1733–1749.
- Kamai R, Abrahamson NA and Silva WJ (2014) Nonlinear horizontal site amplification for constraining the NGA-West2 GMPEs. *Earthquake Spectra* 30(3): 1223–1240.
- Kamai R, Abrahamson NA and Silva WJ (2016) VS30 in the NGA GMPEs: Regional differences and suggested practice. *Earthquake Spectra* 32(4): 2083–2108.
- Kim B, Hashash YMA, Stewart JP, Rathje EM, Harmon JA, Musgrove MI, Campbell KW and Silva WJ (2016) Relative differences between nonlinear and equivalent-linear 1-D site response analyses. *Earthquake Spectra* 32(3): 1845–1865.
- Kramer SL (1996) *Geotechnical Earthquake Engineering* (Prentice-Hall Civil Engineering and Engineering Mechanics Series). Upper Saddle River, NJ: Prentice Hall.
- Ktenidou OJ, Cotton F, Abrahamson NA and Anderson JG (2014) Taxonomy of κ : A review of definitions and estimation approaches targeted to applications. *Seismological Research Letters* 85(1): 135–146.
- Kuncar FA, Bradley BA, Torre C, Rodriguez-Marek A, Zhu C and Lee RL (2024) Comparing and evaluating alternative methods to account for shallow site effects in hybrid broadband ground-motion simulations. *Japanese Geotechnical Society Special Publication* 10(47): 1757–1762.
- Lee RL, Bradley BA, Stafford PJ, Graves RW and Rodriguez-Marek A (2020) Hybrid broadband ground motion simulation validation of small magnitude earthquakes in Canterbury, New Zealand. *Earthquake Spectra* 36(2): 673–699.
- Lee RL, Bradley BA, Stafford PJ, Graves RW and Rodriguez-Marek A (2022) Hybrid broadband ground-motion simulation validation of small magnitude active shallow crustal earthquakes in New Zealand. *Earthquake Spectra* 38(4): 2548–2579.
- Mai PM, Imperatori W and Olsen KB (2010) Hybrid broadband ground-motion simulations: Combining long-period deterministic synthetics with high-frequency multiple S-to-S backscattering. *Bulletin of the Seismological Society of America* 100(5A): 2124–2142.
- McKenna F (2011) OpenSees: A framework for earthquake engineering simulation. *Computing in Science & Engineering* 13(4): 58–66.
- NRC (2021) *Documentation report for SSHAC level 2: Site response*. Technical Report RIL2021-15. Rockville, MD: United States Nuclear Regulatory Commission (US NRC).
- Nweke CC, Stewart JP, Wang P and Brandenberg SJ (2022) Site response of sedimentary basins and other geomorphic provinces in southern California. *Earthquake Spectra* 38(4): 2341–2370.
- Ojeda J, Akinci A, Tinti E, Arriola S and Ruiz S (2021) Hybrid broadband strong-motion simulation to investigate the near-source characteristics of the M6.5, 30 October 2016 Norcia, Italy earthquake. *Soil Dynamics and Earthquake Engineering* 149: 106866.
- Paolucci R, Evangelista L, Mazzieri I and Schiappapietra E (2016) The 3D numerical simulation of near-source ground motion during the Marsica earthquake, central Italy, 100 years later. *Soil Dynamics and Earthquake Engineering* 91: 39–52.
- Paolucci R, Smerzini C and Vanini M (2021) BB-SPEEDset: A validated dataset of broadband near-source earthquake ground motions from 3D physics-based numerical simulations. *Bulletin of the Seismological Society of America* 111(5): 2527–2545.
- Pilz M and Cotton F (2019) Does the one-dimensional assumption hold for site response analysis? A study of seismic site responses and implication for ground motion assessment using KiK-net strong-motion data. *Earthquake Spectra* 35(2): 883–905.
- Pilz M, Cotton F, Razafindrakoto HNT, Weatherill G and Spies T (2021) Regional broad-band ground-shaking modelling over extended and thick sedimentary basins: An example from the Lower Rhine Embayment (Germany). *Bulletin of Earthquake Engineering* 19(2): 581–603.

- Pretell R, Abrahamson NA and Ziotospolou K (2023) A borehole array data-based approach for conducting 1D site response analyses I: Damping and V_S randomization. *Earthquake Spectra* 39: 1473–1501.
- Razafindrakoto HNT, Bradley BA and Graves RW (2018) Broadband ground-motion simulation of the 2011 Mw 6.2 Christchurch, New Zealand, earthquake. *Bulletin of the Seismological Society of America* 108(4): 2130–2147.
- Razafindrakoto HNT, Cotton F, Bindi D, Pilz M, Graves RW and Bora S (2021) Regional calibration of hybrid ground-motion simulations in moderate seismicity areas: Application to the Upper Rhine Graben. *Bulletin of the Seismological Society of America* 111(3): 1422–1444.
- Rix GJ, Wainaina N, Ebrahimi A, Bachus RC, Limas M, Sancio R, Fait B and Mayne PW and National Cooperative Highway Research Program, Transportation Research Board and National Academies of Sciences, Engineering, and Medicine (2019) *Manual on Subsurface Investigations*. Washington, DC: Transportation Research Board.
- Robertson PK and Cabal K (2022) Guide to cone penetration testing. 7th Edition. Gregg Drilling LLC.
- Rodgers AJ, Pitarka A, Pankajakshan R, Sjögren B and Petersson NA (2020) Regional-scale 3D ground-motion simulations of Mw 7 earthquakes on the Hayward Fault, Northern California resolving frequencies 0–10 Hz and including site-response corrections. *Bulletin of the Seismological Society of America* 110(6): 2862–2881.
- Rodriguez-Marek A, Bommer JJ, Youngs RR, Crespo MJ, Stafford PJ and Bahrampouri M (2021) Capturing epistemic uncertainty in site response. *Earthquake Spectra* 37(2): 921–936.
- Roten D, Olsen KB and Pechmann JC (2012) 3D simulations of M 7 earthquakes on the Wasatch Fault, Utah, part II: Broadband (0–10 Hz) ground motions and nonlinear soil behavior. *Bulletin of the Seismological Society of America* 102(5): 2008–2030.
- Seed HB and Idriss IM (1969) Influence of soil conditions on ground motions during earthquakes. *Journal of the Soil Mechanics and Foundations Division* 95(1): 99–137.
- Seyhan E and Stewart JP (2014) Semi-empirical nonlinear site amplification from NGA-West2 data and simulations. *Earthquake Spectra* 30(3): 1241–1256.
- Seylabi E, Restrepo D, Taborda R and Asimaki D (2021) Deterministic ground motion simulations with shallow crust nonlinearity at Garner Valley in Southern California. *Earthquake Engineering & Structural Dynamics* 50(1): 43–59.
- Shi J (2019) *Improving site response analysis for earthquake ground motion modeling*. PhD Thesis, California Institute of Technology, Pasadena, CA.
- Shi J and Asimaki D (2017) From stiffness to strength: Formulation and validation of a hybrid hyperbolic nonlinear soil model for site-response analyses. *Bulletin of the Seismological Society of America* 107(3): 1336–1355.
- Smerzini C, Paolucci R and Stupazzini M (2011) Comparison of 3D, 2D and 1D numerical approaches to predict long period earthquake ground motion in the Gubbio plain, Central Italy. *Bulletin of Earthquake Engineering* 9(6): 2007–2029.
- Smerzini C, Pitilakis K and Hashemi K (2017) Evaluation of earthquake ground motion and site effects in the Thessaloniki urban area by 3D finite-fault numerical simulations. *Bulletin of Earthquake Engineering* 15(3): 787–812.
- Stewart JP, Afshari K and Goulet CA (2017) Non-ergodic site response in seismic hazard analysis. *Earthquake Spectra* 33(4): 1385–1414.
- Taborda R, Bielak J and Restrepo D (2012) Earthquake ground-motion simulation including nonlinear soil effects under idealized conditions with application to two case studies. *Seismological Research Letters* 83(6): 1047–1060.
- Teague D, Cox B, Bradley B and Wotherspoon L (2018) Development of deep shear wave velocity profiles with estimates of uncertainty in the complex interbedded geology of Christchurch, New Zealand. *Earthquake Spectra* 34(2): 639–672.
- Thompson EM, Baise LG, Kayen RE and Guzina BB (2009) Impediments to predicting site response: Seismic property estimation and modeling simplifications. *Bulletin of the Seismological Society of America* 99(5): 2927–2949.

- Thompson EM, Baise LG, Kayen RE, Morgan EC and Kakla manos J (2011) Multiscale Site-response mapping: A case study of Parkfield, California. *Bulletin of the Seismological Society of America* 101(3): 1081–1100.
- Thompson EM, Baise LG, Tanaka Y and Kayen RE (2012) A taxonomy of site response complexity. *Soil Dynamics and Earthquake Engineering* 41: 32–43.
- Thomson EM, Bradley BA and Lee RL (2020) Methodology and computational implementation of a New Zealand Velocity Model (NZVM2.0) for broadband ground motion simulation. *New Zealand Journal of Geology and Geophysics* 63(1): 110–127.
- Thomson WT (1950) Transmission of elastic waves through a stratified solid medium. *Journal of Applied Physics* 21(2): 89–93.
- Walling M, Silva W and Abrahamson N (2008) Nonlinear site amplification factors for constraining the NGA models. *Earthquake Spectra* 24(1): 243–255.
- Williams T and Abrahamson N (2021) Site-response analysis using the shear-wave velocity profile correction approach. *Bulletin of the Seismological Society of America* 111(4): 1989–2004.
- Wotherspoon LM, Orense RP, Bradley BA, Cox BR, Wood C and Green RA (2015) *Geotechnical characterisation of Christchurch strong motion stations*. Earthquake Commission Report Project No. 12/629, Version 3. Christchurch: University of Auckland & EQC.
- Xu B, Rathje EM, Hashash Y, Stewart J, Campbell K and Silva WJ (2020) κ_0 for soil sites: Observations from KiK-net sites and their use in constraining small-strain damping profiles for site response analysis. *Earthquake Spectra* 36(1): 111–137.
- Yang Z, Elgamal A and Parra E (2003) Computational model for cyclic mobility and associated shear deformation. *Journal of Geotechnical and Geoenvironmental Engineering* 129(12): 1119–1127.
- Yang Z, Lu J and Elgamal A (2008) OpenSes soil models and solid-fluid fully coupled elements. User's Manual, 2008 Ver 1.0. Department of Structural Engineering, University of California, San Diego. http://www.soilquake.net/opensees/OSManual_UCSD_soil_models_2008.pdf
- Yee E, Stewart JP and Tokimatsu K (2013) Elastic and large-strain nonlinear seismic site response from analysis of vertical array recordings. *Journal of Geotechnical and Geoenvironmental Engineering* 139(10): 1789–1801.
- Zhu C, Cotton F, Kawase H, Haendel A, Pilz M and Nakano K (2022) How well can we predict earthquake site response so far? Site-specific approaches. *Earthquake Spectra* 38(2): 1047–1075.